

REVIEW ARTICLE

# X-ray absorption spectroscopy (EXAFS and XANES) at surfaces

To cite this article: D Norman 1986 *J. Phys. C: Solid State Phys.* **19** 3273

View the [article online](#) for updates and enhancements.

## REVIEW ARTICLE

# X-ray absorption spectroscopy (EXAFS and XANES) at surfaces

D Norman

SERC Daresbury Laboratory, Warrington WA4 4AD, UK

Received 17 January 1986

**Abstract.** X-ray absorption spectroscopy is now being applied to the study of a wide range of surface structures. The modulation of the absorption coefficient as a function of photon energy, caused by photo-electron scattering, contains information on the local geometric structure around the absorbing atom. Far above an absorption edge, in the EXAFS (extended x-ray absorption fine structure) regime, single scattering usually applies and near-neighbour distances ( $R$ ) and coordination numbers ( $N$ ) can readily be obtained. Some of the factors influencing the scattering and thus an accurate determination of  $R$  and  $N$  are critically discussed. The usefulness of surface EXAFS (SEXAFS) is illustrated by reviewing measurements on the oxidation of aluminium, the adsorption of Te and I on silicon and germanium, the clean surface structure of ion-bombarded silicon, and the ionic-covalent transition in sub-monolayer coverages of caesium adsorbed on silver. Near to the absorption edge, the XANES (x-ray absorption near edge structure), also called NEXAFS (near-edge x-ray absorption fine structure), is often complicated by multiple-scattering effects and may in consequence produce a spectrum rich in structure but awkward to interpret. The atomic adsorption of oxygen on nickel is given as an example. However, for molecular adsorbates, the XANES is often dominated by intra-molecular scattering, and may then quite simply yield the molecular orientation and intra-molecular distances, and hence details of the bonding to the surface. These ideas are illustrated by the adsorption of various carbon- and oxygen-containing small molecules.

## 1. Introduction

X-ray absorption spectroscopy has a long and venerable history in the study of solids (see, e.g., Mott and Jones 1936). Its application to surfaces is, however, a fairly recent phenomenon, brought about partly by the massive rise in interest in surface science and partly by the availability of intense, tunable sources of x-rays in the form of electron storage rings.

When studying the adsorption of atoms and molecules at solid surfaces one is interested in obtaining information on the electronic structure and on the local geometric structure around the adsorbate. The electronic structure can be deduced by a number of techniques, of which photo-emission has been by far the most successful, but determination of the geometric (crystallographic) structure is rather more difficult. Comparison of the results of multiple-scattering calculations with data from low-energy electron diffraction (LEED) experiments (Jona 1978) has enabled several hundred surface structures to be determined over the last few years, but the application of this technique

is limited to single-crystal substrates with atoms or molecules adsorbed in a regular, simple pattern possessing long-range order within the adsorbate plane. Surface extended x-ray absorption fine structure (SEXAFS), in principle, does not suffer from those limitations and is fast becoming the technique of choice for the determination of the local structure of adsorbates at surfaces. Extensions of the method have shown that it can also be applicable to clean surfaces. Studies of the x-ray absorption near edge structure (XANES), also called NEXAFS (near-edge x-ray absorption fine structure), have proved of some interest for atoms on surfaces, but turn out to be particularly useful for molecular adsorbates, where the molecular orientation and intra-molecular bond length can often be readily obtained, thus providing valuable details of molecular bonding at surfaces.

This Review gives a selection of the applications of x-ray absorption spectroscopy at surfaces, concentrating on the physical principles involved, and showing the wide variety of possible uses of these techniques. I have chosen to do this by discussing some interesting examples, selected to illustrate different aspects of surface science. It is emphasised that this is a personal selection, and a complete review of all SEXAFS measurements may be found elsewhere (Stöhr 1986). Some of the examples of molecular chemisorption may appear to sit uneasily in a journal of solid state physics, but they are included to demonstrate the application of basic physical principles to the interdisciplinary subject of surface science.

## 2. Basic physics of x-ray absorption

The basic physical processes involved in x-ray absorption are depicted schematically in figure 1. The energies of the discrete core electron levels are determined uniquely by the atom type, so tuning the photon energy to a particular core level immediately gives an *atom-specific* probe. When its photon energy is greater than the binding energy of the core level, a photon may be absorbed, giving its energy to a photo-electron. In a molecule or solid, part of the photo-electron wave may be back-scattered from neighbouring atoms, with consequent modulation of the matrix element for the absorption. The back-

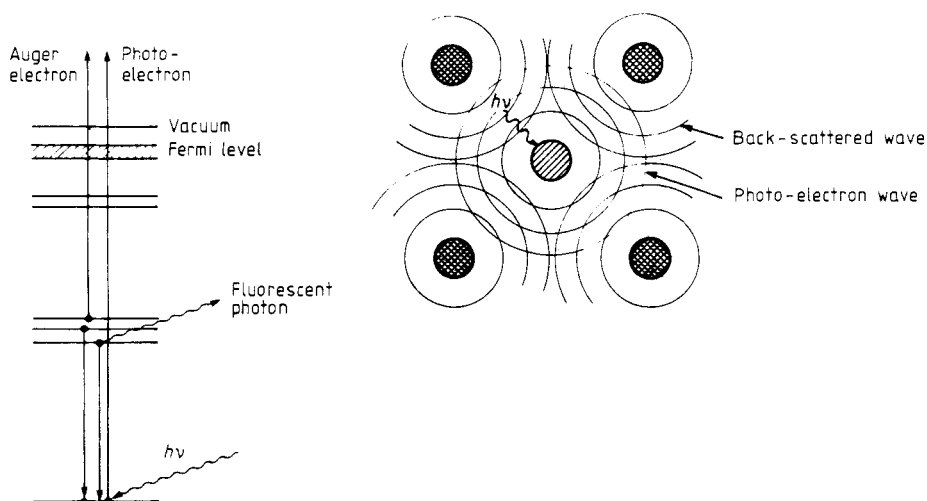
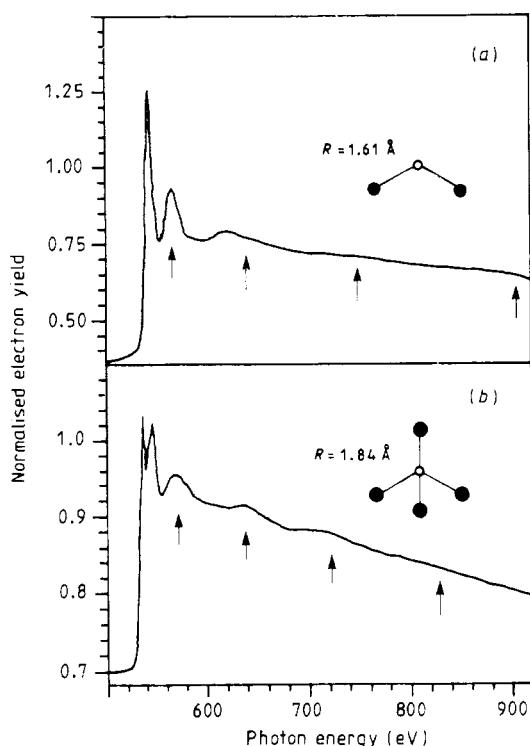


Figure 1. A schematic diagram of photon absorption and photo-electron scattering.



**Figure 2.** X-ray absorption spectra above the O K edge in bulk SiO<sub>2</sub> (a) and Cu<sub>2</sub>O (b). The oscillatory structure (EXAFS) displays a shorter period for the longer bond length in Cu<sub>2</sub>O, and its amplitude is greater with photo-electron back-scattering from more, and heavier, neighbouring atoms.

scattered wave will interfere with the outgoing wave, and the interference may be constructive or destructive, depending on the wave-vector and distance.

Typical x-ray absorption spectra are shown in figure 2 (Stöhr *et al* 1980a), where it is seen that there is a strong step-like rise in absorption as the photon energy is increased through a core electron energy level, followed by oscillatory structure in the absorption coefficient above the edge. The oscillatory part of the spectrum ( $\chi(h\nu)$ ) is readily extracted:

$$\chi(h\nu) = (\mu - \mu_0)/(\mu_0 - \mu_*)$$

where  $\mu$  is the total absorption,  $\mu_0$  is the monotonic free-atom-like absorption and  $\mu_*$  is the background corresponding to absorption in the substrate and at core levels other than the one being studied. The denominator is just the 'edge jump', the step height at the absorption edge, and normalisation to this ensures that, for instance, effects due to varying collection geometry in polarisation-dependent experiments are correctly dealt with. A simplified expression for absorption at an initial state with zero angular momentum (K or L<sub>1</sub> edge) gives the modulated part of the spectrum as a function of the photo-electron wave-vector  $k(\chi(k))$ :

$$\chi(k) = - \sum_i \frac{N_i^*}{kR_i^2} f_i(k) e^{-2\sigma_i^2 k^2} e^{-2R_i/\lambda(k)} \sin(2kR_i + \varphi_i(k)). \quad (1)$$

The exponential terms contain the Debye–Waller-like vibrational softening and the damping due to the finite coherent path length of the photo-electrons. The summation index  $i$  refers to all neighbouring shells separated from the central (absorbing) atoms by a distance  $R_i$ , and  $\varphi_i$  is the phase-shift experienced by the photo-electron escaping the potential of the absorbing atom and being back-scattered by a neighbour. The wave-vector  $k$  is related to the photon energy  $h\nu$  by the simple expression for free electrons

$$\hbar^2 k^2 = 2m(h\nu - E_0)$$

where  $E_0$  corresponds to the zero of the photo-electron kinetic energy scale. The back-scattering amplitude  $f_i(k)$  of a neighbour depends strongly on its atomic number and the back-scattering signature as a function of  $k$  may be helpful in distinguishing different neighbouring atom types, at least to the level of discriminating between atoms in different rows of the periodic table. The effective coordination number  $N_i^*$  is given by

$$N_i^* = 3 \sum_{j=1, N_i} \cos^2 \theta_j \quad (2)$$

where  $\theta_j$  is the angle between the polarisation vector  $\mathbf{E}$  and the vector  $\mathbf{r}_{ij}$  from the central atom to the  $j$ th atom in the  $i$ th shell. Thus the EXAFS  $\chi(k)$  due to the  $i$ th shell of neighbours vanishes if  $\mathbf{E}$  is perpendicular to  $\mathbf{r}_{ij}$  and has maximum amplitude when  $\mathbf{E}$  is parallel to  $\mathbf{r}_{ij}$ . This polarisation dependence usually vanishes by angular averaging in bulk (isotropic) samples but for surface studies, where  $\mathbf{r}_{ij}$  is often well defined, the polarisation dependence of  $N_i^*$  is one of the best methods of determining an adsorption site. For single-crystal surfaces the orientation of  $\mathbf{E}$  with respect to the inter-nuclear axis is defined by a compound angle involving  $\theta$ , the angle of the surface plane to the electric vector, and  $\varphi$ , the azimuthal angle within the surface plane. The  $\varphi$ -dependence vanishes for systems of high local symmetry, but has been experimentally observed (see, e.g., Döbler *et al* 1984) for adsorption onto the FCC (110) plane which is only twofold rotationally symmetric. An important practical point is that experiments with adsorbates on single-crystal surfaces may be hampered by Bragg diffraction of the incident x-rays within the bulk of the crystal, which causes large modulations of the photon absorption coefficient, thus making certain ranges of  $\theta$  inaccessible to study. Since the Bragg condition also depends on the azimuthal angle, variation of  $\varphi$  can help to eliminate these spikes.

The total phase-shift  $\varphi_{ij}(k)$  for scattering between a pair of atoms  $i$  and  $j$  can be expressed as

$$\varphi_{ij}(k) = 2\delta_i(k) + \varphi_j(k)$$

where  $\delta_i$  is the central- (absorbing) atom phase-shift, which enters into the expression twice since the photo-electron experiences this shift both on its way out and on its way back to the absorber atom, and  $\varphi_i$  is the phase-shift experienced by the photo-electron on being back-scattered from the neighbouring atom.

It is clear from equation (1) that the key to accurate determination of bond distances from SEXAFS is the knowledge of phase-shifts  $\varphi(k)$ . There are two principal ways of obtaining phase-shifts: by calculation (according to any of the prescriptions of solid state physics), or by transferring them from 'model compounds'. Electron scattering, except at very low energies, should be mainly by the core electrons, and thus depend little on the detailed atomic environment. Scattering phase-shifts for a particular pair of absorbing and back-scattering atoms should therefore be transferable from a suitable model compound to the unknown system under investigation. The idea of phase-shift transferability (Citrin *et al* 1976) has been tested for a wide range of systems, and appears

to work very well. This transferability can readily be justified: out of the total phase term  $(2kR + \varphi)$ ,  $2kR$  may be as much as 50 rad,  $\varphi$  may be of the order of 5 rad, whereas the differences in  $\varphi$  between different compounds may be of the order of 0.1 rad. These differences due to different valence charge arrangements are thus relatively insignificant. The photon absorption leaves a core hole on the central atom, and thus the potential around this atom is rather different from its ground state; this effect is modelled by making the so-called ' $Z + 1$ ' approximation, taking the potential to be that of the next-heaviest atom, with an appropriate core hole. This crude approximation seems to simulate the central-atom phase-shift reasonably well, and is justifiable because the charge of the inner core hole draws in the valence electrons in much the same way as an extra atomic charge does.

There are various assumptions underlying the simplified EXAFS expression (equation (1)), and these should be borne in mind and critically examined for each application of the technique. These effects have been extensively discussed in the literature (see, e.g., Stern *et al* 1980, Lee *et al* 1981, Hayes and Boyce 1982) and here I merely summarise them, with particular emphasis on problems that may apply especially to surface studies.

The simple theory assumes contributions from single scattering only. Far from the edge, in the EXAFS regime, photo-electron mean free paths (MFPS) tend to be short and scattering amplitudes are weak, and a single-scattering picture is usually valid. Near to the edge, in the XANES region, electron MFPS tend to be longer and scattering strengths are greater, making multiple-scattering effects more important. There is no well defined dividing line between the two regions of the spectrum but there are real physical differences between the predominant scattering events giving the modulation of the core hole absorption matrix element in the XANES regime and the EXAFS regime. The key to this is that, at high electron kinetic energies, strong scattering only occurs in the forward or backward directions; only at low energies is scattering through other angles at all probable. Multiple-scattering effects may sometimes be important in the 'EXAFS' part of the spectrum, most notably when atoms are close to collinear (Lee and Pendry 1975). Then, the scattering contribution from the distant atom is considerably enhanced because the electron wave becomes focused by the potential of the intervening atom, a circumstance often confusingly referred to as 'shadowing'. The effect is that the 'shadowed' atoms appear to be at a much reduced shell radius and a very much larger coordination number than the real values. This is obviously most likely in highly symmetric crystalline samples, such as the single crystals that are used as substrates in many surface-science experiments, but this atomic collinearity does not usually persist when the crystal is viewed radially outwards from an adsorbate atom. Nearest-neighbour information can never be affected by multiple scattering, since there is no possible electron path shorter than the direct single-scattering route.

The formula assumes that the size of the back-scattering atom is small compared with the distance from the central atom, so the electron wave propagating from the absorber may be treated asymptotically as a plane wave. This small-atom approximation is worst for the near-neighbour atoms at low  $k$  and becomes better at higher  $k$  as the effective size of the atom involved in the back-scattering is reduced for more energetic electrons. For surfaces, many adsorbate-substrate distances are rather short, giving EXAFS 'wiggles' of a long period, and absorption edges—particularly at low energies—occur fairly close together, leading to a limited photon energy range in the data, and a low information content. The rapid decrease in absorption cross section and the low surface Debye temperature often encountered also conspire to limit the useful range of SEXAFS. This means that it can be important to extend analysis as far as possible into the low- $k$  part of

the surface EXAFS spectrum, and thus a full curved-wave theory, taking into account the curvature of the electron wavefront at the back-scatterer, can be particularly useful.

Equation (1) contains the Debye–Waller-like term  $\exp(-2\sigma_l^2 k^2)$ , accounting for vibrational disorder. This derives from the harmonic approximation and is usually justified at low temperatures such that  $\sigma_l k \ll 1$ . When anharmonic effects are important, a more accurate expression for the disorder has to be used, including higher-order terms in the pair distribution function. In addition to these effects on the EXAFS amplitude, anharmonic vibrations can lead to an incorrect determination of *distance*, since a phase term is introduced by odd moments of the distribution function. (In fact, anharmonicity to lowest order affects only the phase and not the amplitude of  $\chi(k)$  (Eisenberger and Brown 1979).) Expressed another way, an atom vibrating in an anharmonic potential has a positional probability distribution function that is asymmetric with a more abrupt edge at distances shorter than the mean and thus has Fourier components from its sharper edge extending farther throughout  $k$ -space. Since the low- $k$  range (the XANES) is inevitably lost from the EXAFS analysis, these Fourier components are missing, leading to an apparent mean distance shorter than the real value. Therefore, measurements should preferably be carried out at low temperatures, and ideally should be performed at a range of different temperatures to check for anharmonicity, provided that the temperature can be varied without affecting the scientific problem that is being addressed. A further contribution to the disorder term can arise from static disorder, where even at zero temperature a range of sites is occupied, as may happen particularly with amorphous or glassy samples. Note that the Debye–Waller factor derived from long-range diffraction techniques such as x-ray diffraction or LEED is not the same as the  $\sigma$  in equation (1), since EXAFS samples directly the distance between adjacent atoms and thus  $\sigma$  is a measure of *correlated* motion. Since nearby atoms tend to move in sympathy with the central atom, the mean squared relative displacement measured by EXAFS tends to be smaller than the uncorrelated Debye–Waller factor between atoms far distant from each other. Long-wavelength phonons, for example, will give a much smaller contribution in EXAFS than in diffraction. Finally, vibrational amplitudes at a surface may well differ from those in the bulk (Brennan 1982), and in principle SEXAFS could be used to determine the surface phonon spectrum of the adsorbate–substrate system.

The simple equation depicts the scattering in essentially a one-electron model, with some multi-electron effects included via the finite mean free path for coherent scattering. In other words, the outgoing wave lasts only for a finite time, this lifetime limiting the detail that can be found in the EXAFS signal. The lifetime of the core hole created in the photo-absorption event may also be significant: for deep-lying electron shells in heavy atoms, the hole lifetime may be so short that the hole has, in effect, disappeared before the back-scattered wave can coherently interfere with it. Fortunately this is not a problem for edges lying below 10 keV, the region most readily accessible for SEXAFS measurements.

Other many-body effects manifest themselves in a reduction of the EXAFS amplitude, relative to the total absorption. Some of the photons absorbed may produce not a single electron ejected from the atom but may instead lead to more complicated effects involving sharing the kinetic energy between the excited atom and the ejected electron ('shake-up'), or between several electrons ('shake-off'), or other collective excitations such as plasmons. The proportion of all the photo-absorption events contributing towards the EXAFS is typically between 0.6 and 0.8, but this factor, usually written  $S_0^2(k)$ , has a  $k$ -dependence (Stern *et al* 1980): for energetic photo-electrons the 'sudden approximation' is valid but lower-energy electrons remain in the vicinity of the core hole

for a longer time. In the adiabatic limit of zero-energy electrons emitted, there are no many-body effects and the independent particle model is accurate. The  $k$ -dependence of  $S_0^2$  takes account of this variation in timescale. It has also been suggested (Pettifer 1979) that at least part of this apparent  $k$ -dependence of amplitude may be due to neglect of the curvature of the wavefront at lower  $k$ . Fortunately, from the viewpoint of using EXAFS as a structural tool,  $S_0^2(k)$  has been found to depend only on the type of absorbing atom, not on its chemical environment, thus allowing the pure atomic values to be used, or values transferred from model compounds.

For absorption at a p-like initial state ( $L_2$  or  $L_3$  edge) the equations become rather more complicated, since optical (dipole) selection rules allow transitions to final states of both s and d symmetry. The equivalent expression to equation (1) is

$$\chi(k) = \sum_i \frac{1}{kR_i^2} f_i(k) e^{-2\sigma_i^2 k^2} e^{-2R_i/\lambda(k)} \frac{M^*}{(M_{21}^2 + \frac{1}{2}M_{01}^2)} \quad (3)$$

where

$$M^* = \frac{1}{2} \left( 1 + 3 \sum_{j=1, N_i} \cos^2 \theta_j \right) M_{21}^2 \sin(2kR_i + \varphi_2^i(k)) + \left( 1 - 3 \sum_{j=1, N_i} \cos^2 \theta_j \right) \\ \times M_{01} M_{21} \sin(2kR_i + \varphi_{02}^i(k)) + \frac{1}{2} M_{01}^2 \sin(2kR_i + \varphi_0^i(k))$$

with  $M_{21}$  and  $M_{01}$  the appropriate matrix elements for  $p \rightarrow \epsilon d$  and  $p \rightarrow \epsilon s$  transitions respectively. It is known from theory (Teo and Lee 1979) and experimental measurements (Heald and Stern 1977), that  $|M_{01}/M_{21}| \approx 0.2$  thus making the d wave dominant over the s wave by a factor of about 50 (via the term  $M_{21}^2/2M_{01}^2$ ): so, for most purposes, the s-wave emission may be ignored. The awkward phase-shift term  $\varphi_{02}^i(k) = \delta_0(k) + \delta_2(k) + \varphi^i(k)$  corresponds to emission of a d wave and back-scattering of an s wave or vice versa. The coefficient of this term in equation (3) vanishes by angular integration for isotropic (cubic, amorphous or polycrystalline) samples, so the  $L_{2,3}$ EXAFS amplitude and phase-shift are simply obtained. However, this cross-term may be quite important for anisotropic systems, such as surfaces, and its effect has been extensively discussed (Stöhr and Jaeger 1983, Citrin 1985). There should be little significant shift in distance, except possibly for some onefold-coordinated surface species, but the effect on amplitudes can be more troublesome, particularly in modifying their polarisation dependence, where equation (2) may now be approximated by

$$N_i^* = \left( \frac{1}{2} + \frac{M_{01}}{M_{21}} \right) N_i + 3 \left( \frac{1}{2} - \frac{M_{01}}{M_{21}} \right) \sum_{j=1, N_i} \cos^2 \theta_j. \quad (4)$$

Note that the polarisation asymmetry is less pronounced than for K or  $L_1$  edges, being weakened by the angular independence of the first term.

It is clear from equations (1) and (3) that EXAFS is a local probe, sampling only short-range order around the absorbing atom, and this is the key to its wide applicability. Note, however, that the technique samples all absorbing atoms of the same type, and averages over them, so good structural information can only be obtained where the central (absorbing) atoms uniquely occupy equivalent sites.

### 3. Experimental arrangement and data analysis

This Article is not intended to be a working manual for the prospective SEXAFS exper-



imeter, so only a brief outline is given in this section. The primary requirement for surface x-ray absorption studies is a photon beam that is intense ( $>10^{10}$  photons  $\text{s}^{-1}$ ), monochromatic (about 0.5–5 eV resolution), linearly polarised, tunable over a wide range (about 250–10000 eV), and preferably in ultra-high vacuum to enable experiments on well characterised surfaces. The only source with these properties is synchrotron radiation with a suitable monochromator. Rather few facilities for x-ray absorption measurements at surfaces are currently available, and details are in the literature (see, e.g., Stöhr *et al* 1980a, Hussain *et al* 1982, MacDowell *et al* 1986).

Although the details of the photon beam-line are not given here, the difficulties in this area should not be under-estimated, and in order to achieve reliable SEXAFS results it is essential, in my view, to have a good understanding of the problems in obtaining and monitoring collimated monochromatic light. Indeed Stöhr (1986) has emphasised that 'SEXAFS measurements cannot be performed by treating everything but the sample chamber as a black box'.

The experiment then consists of measuring the intensity of photons incident on the sample, and the proportion of them that is absorbed, as a function of photon energy. There are various ways of obtaining the x-ray absorption coefficient of the system under study. The ratio of the flux transmitted through a sample to that incident on it directly gives the absorption coefficient; however, this method is not surface-sensitive, since the overwhelming majority of photons is absorbed in the bulk of the material, and the top layers contribute very little to the total absorption. The only successful surface EXAFS measurements performed in transmission mode have been on samples created with an artificially enhanced surface area (see, e.g., Heald and Stern 1978), but industrial catalysts are usually manufactured in such forms and their importance and sensitivity to the details of the surface should not be under-estimated. Most surface EXAFS experiments have involved detection of the x-ray absorption coefficient by indirect means. The core hole created is subsequently annihilated, either by fluorescence, with emission of another photon, or in the Auger process, with emission of an Auger electron. Since these processes are directly linked to the filling of the core hole, and their relative probabilities are dependent only on the type of atom (Bambynek *et al* 1972), a measurement of either of these indirect events generally can serve as a monitor of the photon absorption coefficient. Noguera and Spanjaard (1981) have pointed out that the Auger yield may not always be simply proportional to the absorption cross section, owing to interference effects between the two holes present in the absorption/Auger event, but fortunately these effects seem to be negligible in practice.

The most obvious way to measure the absorption coefficient of surface atoms is by detection of the Auger electrons. Auger yields are greater than 0.5 for the K edges of atoms with  $Z < 31$ , and for the L edges of all atoms. Adsorbates on surfaces typically contain light atoms (C, N, O, S etc) for which Auger emission probabilities are high. The Auger emission is atom-specific, with a kinetic energy characteristic of the binding energies of the levels involved. Auger-yield SEXAFS is thus readily monitored by using an electron energy analyser, working at a fixed kinetic energy, and scanning the photon energy. Note, however, that direct photo-emission peaks from various core levels, either in the adsorbate or the substrate, may be swept through the analysing energy 'window', causing almost insurmountable problems in data collection when this happens.

Electron mean free paths are short, and electrons can emerge elastically only from near the surface. Put another way, almost all Auger (and photo-) electrons produced within the bulk will lose energy on their way towards the surface, through electron-electron, electron-plasmon, electron-phonon and other inelastic scattering processes.

The total number of electrons ( $\gamma$ ) per incident photon created in a depth  $l$  of a solid with absorption coefficient  $\mu$  is  $\gamma = 1 - \exp(-\mu l)$ . However, for photon energies  $h\nu \geq 50$  eV, the photon absorption coefficient  $\mu \geq 1000 \text{ \AA}^{-1}$ , and  $l \approx 50\text{--}100 \text{ \AA}$  (see figure 3) so  $\mu l \ll 1$  and thus  $\gamma \approx \mu l$ . Since  $\gamma$  is proportional to  $\mu$  we can use the total electron yield ( $\gamma$ ) as a measure of photon absorption (Lukirskii and Brytov 1964). However, it should be noted that the total yield is dominated by low-energy electrons for which  $l \approx 50\text{--}100 \text{ \AA}$ , so potentially *bulk* information is obtained, and surface EXAFS is available only if the surface atoms have an absorption edge within the range of photon energies used. Total electron yield should be the detection method employed for most bulk EXAFS measurements in the soft x-ray region where measurements generally have to be performed *in vacuo*.

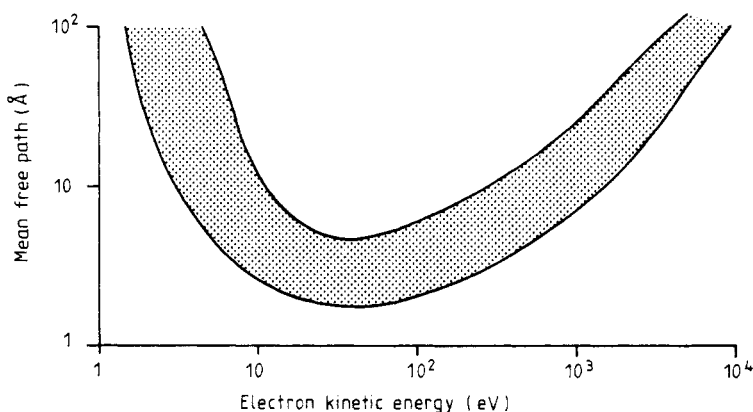


Figure 3. The mean free paths of electrons in most solids fall within the shaded region.

It might be thought that measurement of the yield of the directly emitted photo-electrons would also serve as a monitor of the photon absorption coefficient, but it has been shown theoretically (Lee 1976) that measurement of the photo-electron yield does *not* give EXAFS. This is because the energy of the photo-electrons is changing as the photon energy is scanned, and thus the diffraction effects experienced by the *collected* electrons on their way out of the solid and into the detector are also changing. (This diffraction is the basis of the photo-electron diffraction techniques for determining surface structures (Woodruff *et al* 1978, Kevan *et al* 1978), and should not be confused with the 'internal' photo-electron diffraction effects giving rise to the EXAFS.) Only if the detector measures all  $4\pi$  sr does the photo-electron yield average out to EXAFS, and clearly this is impossible with any external detector, but this may be achieved in studying bulk polycrystalline samples (Rothberg *et al* 1984), where the sample itself may do the averaging. This troublesome photo-electron diffraction effect cannot occur with Auger electrons since their kinetic energy is fixed. Thus, although a fixed electron detector collects a finite solid angle, the diffraction of outgoing Auger electrons into this angle does not change as a function of photon energy.

Of course the direct photo-electrons are also contributing to the *total* yield. However, the elastic photo-electrons have smaller kinetic energies than the Auger electrons, and the Auger electrons thus produce more scattered low-energy electrons: total yield thus tends to be dominated by inelastically scattered Auger electrons, justifying its

proportionality to the photon absorption coefficient. Higher-energy photo-emission peaks can occasionally cause problems in using the total electron yield to monitor the absorption. The technique of partial electron yield has been developed to obviate this difficulty, in which only electrons with energy greater than a set level are detected. This electron kinetic energy level is determined by the desire to keep major direct photo-emission lines out of the set energy range for all values of photon energy to be used in the absorption experiment. Regardless of which mode of electron detection is employed, it is reassuring that the same phase, and thus bond length information, is measured by each method, although the amplitudes may not be transferable between spectra recorded in different ways, due to inelastic and secondary photo-electron contributions (Stöhr *et al* 1984b).

Although their yield may be low, detection of fluorescent photons can also be used to measure SEXAFS. It is not surprising that this method works for heavy atoms on light substrates, where the background signal would be expected to be low, for instance gold on silicon (Heald *et al* 1984): in these experiments surface sensitivity was enhanced by using an extremely small grazing angle for the incident photons, which unfortunately necessitates very large samples whose homogeneity may be difficult to ensure. However it does appear, at first sight, to be rather unexpected that fluorescence yield would be successful for some of the more typical surface problems involving lighter atoms on heavier substrates. Nevertheless, this has now been achieved in experiments on sulphur on nickel (Stöhr *et al* 1985), which are described in more detail in § 5.4. Here it is shown that there is no need for a grazing-incidence geometry, thus allowing the usual polarisation-dependent spectra to be measured, and furthermore, although the total signal levels are (for sulphur) about a factor of 15 lower than for the Auger yield, the signal-background level is dramatically greater for the fluorescence detection. For most dilute systems the signal-background ratio is the critical figure of merit, rather than the signal-noise ratio, and thus the various electron or photon detection schemes described here should be tested to see which gives the best data in each individual case. The main reason for the signal-background enhancement for this fluorescence measurement is that, at these low photon energies, there are almost no inelastic *photon* events, whereas there are many inelastic *electron* scattering events and the Auger peak thus sits on a significant background. Also, the elastically scattered x-ray background from the substrate strongly decreases with decreasing  $h\nu$ . It could be highly advantageous to monitor surface EXAFS by photon detection since (with suitable windows) experiments may then be performed with the sample in a high-pressure cell, rather than the high vacuum needed for electron detection, and surface reactions could then be followed *in situ*.

Attempts have also been made to record SEXAFS spectra by measuring the change in reflectivity as a function of photon energy. It has been theoretically suggested (Fox and Gurman 1980) that, at angles below that for critical reflection, this method should detect just the phase of the imaginary part of the refractive index, i.e. EXAFS. However, experiments (Martens and Rabe 1980) showed that this only strictly applied at angles well below the critical angle and that in general the reflectivity EXAFS differs from absorption EXAFS because of a phase and amplitude contribution from the *real* part of the refractive index, giving an additional phase-shift and amplitude correction. Although in principle these terms can be calculated from the optical constants, in practice they are unlikely to be sufficiently well known, especially in the presence of different adsorbed layers.

One other process that may be physically linked to photon absorption at a core level

is the desorption of ions from a surface. Depending on the timescales and localisation of the Auger filling of the core hole, and the screening at the surface, it is possible for a surface atom to be left in an electrostatically unfavourable charge state, leading to its expulsion from the surface as a positive ion in the process graphically described as the 'Coulomb explosion'. This mechanism for photon-stimulated ion desorption (PSID) is considered to be most likely for ionic solids such as the maximal-valency transition-metal oxides (Knotek and Feibelman 1978), but has also been observed for adsorbates on surfaces (see the review by Knotek 1984). The Auger transition annihilating the core hole may be either intra- or inter-atomic, so desorption of an adsorbed atom may proceed via photon absorption at the adsorbate itself or at a substrate atom to which the adsorbate is directly bonded: the range of wavefunction overlap ensures that more distant atoms cannot be involved. PSID is inherently very surface-sensitive since any ions created within the bulk are almost inevitably re-neutralised on their way to the surface. PSID has been successfully used in only one SEXAFS experiment (Jaeger *et al* 1980), where the desorption of  $O^+$  ions from the  $\alpha$ -phase of oxygen on Mo(100) was monitored, and hence the surface structure determined for the molybdenum atoms to which oxygen atoms were bonded before their desorption. There may be difficulties in making a structural determination when indirect desorption mechanisms occur. For instance, problems may be caused (especially in covalently bonded molecules) by multi-electron effects (Jaeger *et al* 1981), and (especially in insulators) by x-ray-induced electron-stimulated desorption, (Jaeger *et al* 1983, Owen *et al* 1986), where the ion desorption is stimulated indirectly by a photo-electron, rather than directly in the original photo-absorption event.

Methods of data analysis will not be discussed in detail here (see, e.g., Lee *et al* 1981). The basic idea is to disentangle from the experimental spectrum the information on bond length and coordination number, bearing in mind the various possible physical problems outlined above. Several of the components of the EXAFS equation are highly correlated, with the distance, phase-shift and  $E_0$  in one group determining the phase and the amplitude being affected by the coordination number, Debye-Waller factor,  $S_0^2$  and  $\lambda$ . In some circumstances the effects of these different terms may be separated by their different  $k$ -dependences. One of the major advantages of SEXAFS over other surface structural techniques is that, when the single-scattering approximation is valid, it is possible to go directly from the experimental spectrum, via Fourier transformation, to a bond length determination. Several examples of how this may be achieved are described in the next section.

## 4. SEXAFS studies

### 4.1. Oxygen on aluminium

This is taken as the first example to indicate the wealth of structural information that may be deduced from a combination of surface EXAFS with other techniques. The interaction of oxygen with aluminium is a classic example of protective oxide formation at metal surfaces, and is of great technological importance in the aerospace industry. From an academic point of view the O-Al system is interesting because the bonding is of simple s-p character, thus enabling *ab initio* theoretical model calculations: several such calculations have been carried out, using a variety of theoretical techniques, for both the earliest stage of the oxidation process—the chemisorption of oxygen on clean Al surfaces—and also for the cases where the oxygen atoms penetrate the aluminium surface layers (see Batra and Kleinman 1984).

Experimentally, the O–Al system has been investigated by a large number of workers using several techniques, including some of the earliest surface EXAFS work (Johansson and Stöhr 1979, Stöhr *et al* 1980b). Photo-emission studies revealed two distinct phases for the initial sorption of oxygen on Al(111) single-crystal surfaces as evident from different shifts of the Al 2p core level. At small oxygen exposures  $\leq 100$  L (1 L =  $10^{-6}$  Torr s) an ordered ( $1 \times 1$ ) configuration was found corresponding to an Al 2p chemical shift of 1.4 eV. Photo-emission and LEED experiments were interpreted to show that oxygen chemisorbs in the threefold hollow site on the Al(111) surface with no Al atom in the second Al layer underneath. This site was also favoured by theoretical calculations. Work-function measurements imply that around monolayer coverage ( $\sim 100$ – $150$  L O<sub>2</sub>) the O atoms are outside the surface. The second phase, which increases with oxygen exposure or temperature, corresponds to an Al 2p core level shift of 2.7 eV relative to clean Al, which is the same as for bulk Al<sub>2</sub>O<sub>3</sub>. Thus this phase, which often accompanies the chemisorbed phase, has been associated with bulk-like oxide formation with penetration of the Al lattice by O atoms.

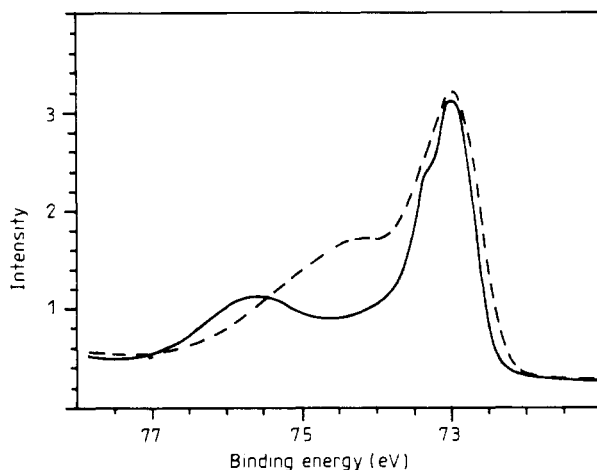


**Figure 4.** Al 2p photo-emission spectra at  $h\nu = 130$  eV for 50 L of oxygen on Al(111) at room temperature (broken curve) and after heating to 200 °C for 10 min (full curve). The spectra were recorded with electron energy analyser resolutions of 0.4 eV and 0.2 eV, respectively.

Exposure of the clean Al(111) surface to 50 L O<sub>2</sub> produces a photo-emission spectrum in the region of the Al 2p level shown by the broken curve in figure 4. The Al 2p level, whose spin–orbit splitting is barely visible with the resolution used here, is accompanied by a shoulder 1.4 eV higher in binding energy, which is the shift characteristic of the chemisorbed oxygen state (Flodström *et al* 1976). Upon heating to 200 °C for 10 min, the photo-emission spectrum given in figure 4 by the full curve is obtained. This spectrum, taken with improved analyser resolution, clearly shows a peak shifted by 2.7 eV from the Al 2p level, with no peak shifted by 1.4 eV. The heating converts the chemisorbed state into a phase exhibiting the same binding energy as bulk Al<sub>2</sub>O<sub>3</sub>. Figure 5 depicts the EXAFS spectra (Norman *et al* 1981) above the oxygen K edge for the two oxygen coverages corresponding to the photo-emission spectra of figure 4, and also from a sample of corundum,  $\alpha$ -Al<sub>2</sub>O<sub>3</sub>, which has a well known mean bond length,  $R_{\text{O-Al}} =$

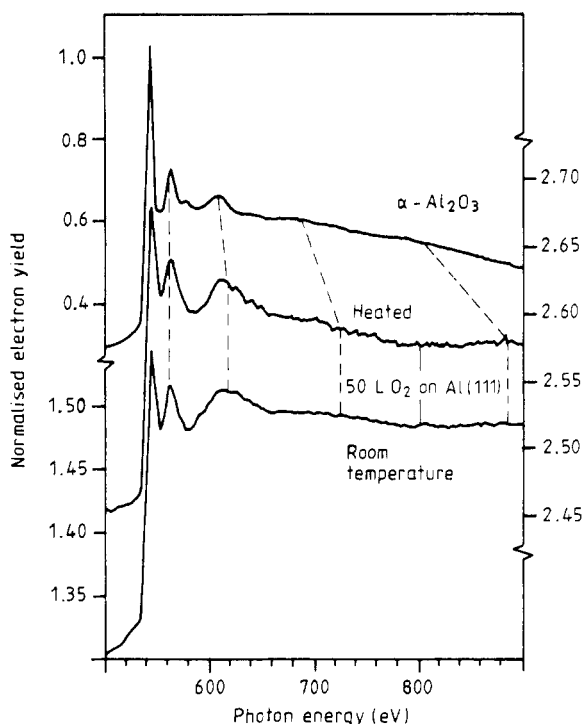


**Figure 5.** EXAFS spectra above the O K edge for  $\alpha$ - $\text{Al}_2\text{O}_3$  (corundum) and 50 L oxygen on Al(111) at room temperature and after heating to 200 °C for 10 min. The lower two spectra were recorded on the same samples as used for figure 4.

1.915 Å. The EXAFS oscillations are nearly sinusoidal (in  $k$ -space) for all three spectra, indicating that the O–Al nearest-neighbour (NN) scattering dominates over more distant neighbour shells. The broken lines join the peaks due to O–Al NN scattering and show just by considering the frequency of the oscillations and without further analysis that the O–Al NN distance is longer for  $\alpha$ - $\text{Al}_2\text{O}_3$  than for the oxygen-exposed Al(111) surface, and that there is essentially no change in bond length between the chemisorbed and the heated surface phases. Fourier transformation and correction by the O–Al scattering phase-shift derived from the bulk  $\text{Al}_2\text{O}_3$  gives values of  $R = (1.76 \pm 0.03)$  Å for the O–Al distance in the chemisorbed phase and  $R = (1.75 \pm 0.03)$  Å for the heated phase. For the chemisorbed state there is strong support of the  $(1 \times 1)$  oxygen overlayer structure suggested previously from LEED and depicted in figure 6(a). As is usually found with chemisorption systems on metal surfaces, the adsorbate (O) atoms are located in positions that are a continuation of the (FCC) stacking of the bulk (Al) lattice. However the inter-planar spacing ( $0.6 \pm 0.1$ ) Å here derived (assuming no relaxation of the surface Al layer) is considerably reduced from the inter-planar separation of 2.33 Å for bulk Al.

The in-plane O–O distance can also be obtained (Stöhr *et al* 1980b) by using the polarisation dependence of the EXAFS. Figure 7 shows the Fourier transforms (FTs) for spectra taken around monolayer coverage at grazing incidence ( $\theta = 11^\circ$ ) and a  $45^\circ$  angle of photon incidence. For  $\theta = 45^\circ$  the electric field vector has a sizable component parallel to the Al(111) surface and the in-plane O–O distance can be observed (peak B) in addition to the O–Al distance (peak A). Peak B yields an O–O distance of  $(2.90 \pm 0.05)$

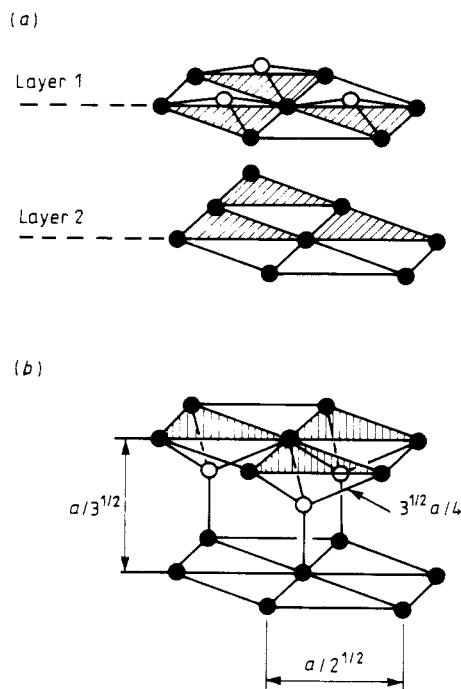


**Figure 6.** (a) Model for the chemisorbed phase of oxygen on Al(111) in the coverage range from one-half to one monolayer; the shaded areas lie directly underneath each other. (b) Model for the oxide-like phase of oxygen on Al(111) in the same coverage range. ●, Al; ○, O.

Å, in excellent agreement with the Al–Al separation of 2.86 Å in the (111) Al surface plane.

For the initial oxide phase the same O–Al bond length is found, within experimental error. This strongly supports the geometry shown in figure 6(b) for this phase, in which an O atom is bonded to four Al atoms as in corundum and  $\gamma$ -alumina and each surface Al atom is bonded to three O atoms. The ideal O–Al bond length for a tetrahedron of Al atoms with an O atom at the centre is 1.75 Å, which is exactly equal to the experimental value. This site can be occupied simultaneously with the chemisorption site without distortion of the lattice, and both chemisorbed and oxide-like phases have previously been observed together (Flodström *et al* 1976). For both phases the O atoms form a  $(1 \times 1)$  configuration with respect to the clean Al(111) surface, which can explain why a sharp  $(1 \times 1)$  LEED pattern persists after relatively high exposures ( $\sim 1000$  L O<sub>2</sub>) corresponding to more than monolayer coverage.

The SEXAFS results for the O–Al bond length  $R = (1.76 \pm 0.03)$  Å in the chemisorbed phase were in gross disagreement with three previous independent LEED investigations (Martinson *et al* 1979, Yu *et al* 1980, Payling and Ramsey 1980) of the same system, which all suggested  $R_{\text{O-Al}} > 2.12$  Å. Re-evaluation of the LEED data showed that they could also be explained by the short bond length derived by SEXAFS and that the previously derived large  $R$ -value might be due to consideration of an insufficiently wide range of values in the LEED calculations, and comparison with an inadequate experimental data set (Jona and Marcus 1980). Further LEED analyses performed sub-

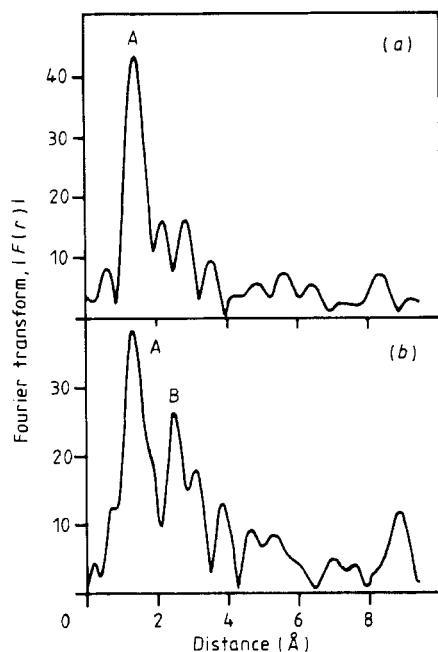


**Figure 7.** (a) The absolute value of the Fourier transform  $|F(r)|$  of the EXAFS signal  $\chi(k)k^2$  above the O K edge for a sample of 100 L O<sub>2</sub> on Al(111) at grazing photon incidence ( $\theta = 11^\circ$ ). Note that the peaks in  $|F(r)|$  are displaced from the true distance by a phase-shift. (b)  $|F(r)|$  of the same sample at  $\theta = 45^\circ$ .

sequent to this SEXAFS result have shown agreement with the SEXAFS-derived distance (Soria *et al* 1981, Neve *et al* 1982).

The same 2.7 eV chemical shift of the Al 2p level is observed for the initial oxide, amorphous alumina and corundum, indicating a very similar total charge transfer from the Al to its neighbouring O atoms in all cases. On the other hand the number  $N$  of oxygen nearest neighbours of the Al atoms is quite different. According to the model (Norman *et al* 1981) the surface Al atoms in the initial oxide phase have  $N = 3$  (see figure 6) while  $N = 6$  for  $\alpha$ -Al<sub>2</sub>O<sub>3</sub>. Amorphous alumina consists of a mixture with some Al atoms coordinated to six O atoms, as in corundum, and some fourfold-coordinated, with the proportions of these two local bonding units varying with the method of preparation. The constant total charge transfer from the Al atoms implies that for different numbers of oxygen neighbours the charge transfer *per oxygen atom* changes: the bond lengths must change to compensate. For predominantly ionic bonds between a given pair of atoms a direct correlation should thus exist between bond length and coordination number. Following Pauling (1960) such a correlation can be easily established. The crystal potential can be approximated in the form

$$V = -A e^2/R + B e^2/R^n$$

where  $A$  is the Madelung constant,  $B$  is a repulsive coefficient,  $e$  is the electronic charge,  $R$  is the nearest inter-ionic distance and  $n$  is the Born exponent, which is found to be in the vicinity of nine for all crystals. Differentiation of this expression leads to an equation for the equilibrium inter-ionic distance  $R_0$ :

$$R_0 = (nB/A)^{1/(n-1)}.$$



For similar crystalline structures the Madelung constant changes very little and the repulsive coefficient is proportional to the number of cation-anion contacts, i.e. the coordination number  $N$ . Hence, for two crystalline forms  $x$  and  $y$ , the ratio of inter-ionic distances is given approximately by

$$R_0^x/R_0^y = (N^x/N^y)^{1/(n-1)}. \quad (5)$$

Thus, taking  $n = 9$  and  $R = 1.915 \text{ \AA}$  for corundum ( $N = 6$ ), it is found that  $N = 3$  for  $R = 1.76 \text{ \AA}$ , in excellent agreement with the earlier discussed model for the initial oxide phase where the derived value  $R = 1.75 \text{ \AA}$  led to the arrangement shown in figure 6 with  $N = 3$ . Equation (5) can now be applied to predict the average coordination number and therefore the ratio of octahedrally to tetrahedrally coordinated Al atoms in various samples of amorphous alumina (Norman *et al* 1981, El-Mashri *et al* 1983).

This model of bond length versus bond order for the oxide phases of aluminium breaks down for the chemisorbed phase which is characterised by about half the chemical shift. In order to exhibit an O-Al bond length of about  $1.76 \text{ \AA}$ , as observed, the surface Al atoms would have to be bonded to half as many (i.e. 1.5) O atoms as in the sub-monolayer oxide phase which shows essentially the same O-Al distance. Alternatively, for a coordination number  $N = 3$  as shown in figure 6 the small charge transfer implied by the  $1.4 \text{ eV}$  chemical shift would lead to a bond length around  $1.92 \text{ \AA}$ , in gross disagreement with the measured value. The observed short bond for the chemisorbed phase can only be reconciled by postulating a considerable covalent character in the chemisorptive bond, thus allowing the O atoms to be drawn closer to the Al surface despite a relatively small net charge transfer. The expected O-Al covalent bond length can be estimated from the sum of the O ( $R_O = 0.66 \text{ \AA}$ ) and Al ( $R_{Al} = 1.26 \text{ \AA}$ ) covalent radii (Pauling 1960) and a correction for the partial ionic character. This latter correction term can be written as  $\Delta R = -c|X_O - X_{Al}|$ , where  $X_O = 3.5$  and  $X_{Al} = 1.5$  are the respective electronegativities and  $c$  is a constant, with values suggested of 0.09 or 0.08. This yields for the covalent O-Al distance  $R = R_O + R_{Al} + \Delta R = 1.74 \text{ \AA}$  or  $1.76 \text{ \AA}$ , in excellent agreement with the SEXAFS value of  $1.76 \pm 0.03 \text{ \AA}$  for the chemisorption bond length.

These SEXAFS measurements were important in determining chemisorption details that were incorrectly deduced from LEED. The ability to follow a reaction through its various stages, in this case from initial chemisorption on a single crystal, through bulk oxide formation and including comparison with amorphous oxides, is uniquely made possible by the local nature of the SEXAFS structural information: no long-range order is necessary.

#### 4.2. Adsorption on semiconductors

It is important technologically that the details of adsorption at semiconductor surfaces are well understood, and it is also of wider theoretical interest, since the bonding mechanisms tend to differ from metal substrates. On metals, bonding is largely non-directional, but the covalent character and consequent directional bonding of semiconductors suggests that a local-orbital approach based on saturation of dangling bonds might be successful in predicting their surface adsorption behaviour. Many experiments (see, e.g., Ludeke and Koma 1975, Pianetta *et al* 1975) have been performed on the surface structure of reconstructed semiconductors using photo-emission, electron energy loss spectroscopy (EELS) and LEED but in none of these studies has it been possible reliably to test this idea. This is in part because no technique other than SEXAFS provides

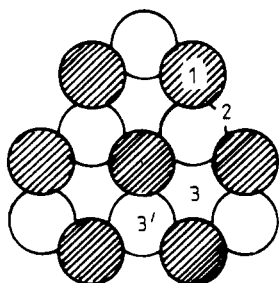


**Figure 8.** The first (shaded) and second (open) layers of an unreconstructed (111) surface with the four highest-symmetry adsorption sites labelled.

the necessary accuracy, but also because all other measurements require long-range order within the overlayer, which may be impossible to achieve. Experiments on the adsorption of Te and I on clean Si(111) ( $7 \times 7$ ) and Ge(111) ( $2 \times 8$ ) surfaces (Citrin *et al* 1982) showed that SEXAFS, not being hampered by either of these limitations, could allow successful testing of the bond saturation arguments.

The data were analysed to give nearest-neighbour and second-nearest-neighbour distances and also effective surface atom coordination numbers, with the polarisation dependence of this latter parameter proving particularly useful in distinguishing between possible adsorption sites. Figure 8 depicts the first- and second-layer atoms in an unreconstructed Si(111) or Ge(111) surface, with the four highest symmetry adsorption sites labelled. The effective surface atom coordination numbers  $N_i^*$  for the different polarisation angles used in the experiment are calculated for each of these four high-symmetry sites and compared with experimental values in table 1. The spectra were measured above the  $L_3$  edges of I and Te and so the polarisation anisotropy is not as great as for absorption at an adsorbate K edge. From these measurements iodine is found to adsorb on both Si(111) and Ge(111) in the atop site (site 1 in figure 8), which is what would be anticipated for a monovalent atom saturating the semiconductor's dangling bond. The second-nearest-neighbour distance on silicon is greater by  $0.1 \text{ \AA}$  than for an unrelaxed ( $1 \times 1$ ) substrate, suggesting outward relaxation of the surface Si atoms, but this effect is not seen on Ge.

The case of tellurium adsorption, however, is distinctly different. We should not be too surprised to find a difference between the adsorption behaviour on Si and Ge in view

**Table 1.** Calculated versus experimental values for  $N_i^*$  for I and Te on Si(111) ( $7 \times 7$ ) and Ge(111) ( $2 \times 8$ ).

	Calculated				Experiment			
	1	2	3	3'	I/Si	I/Ge	Te/Si	Te/Ge
$E^a$	0.7	2.7	5.3	3.0	$0.7 \pm 0.2$	$0.9 \pm 0.2$	$3.0 \pm 0.4$	$2.9 \pm 0.4$
$E^-^b$	1.3	3.0	5.1	3.8	$1.4 \pm 0.3$	$1.8 \pm 0.4$	$2.9 \pm 0.4$	$4.0 \pm 0.5$
$E_-/E^c$	1.9	1.1	1.0	1.3	$2.0 \pm 0.2$	$2.0 \pm 0.3$	$1.0 \pm 0.2$	$1.4 \pm 0.2$

<sup>a</sup> Corresponds to  $\theta = 90^\circ$ .

<sup>b</sup> Corresponds to  $\theta = 35^\circ, 40^\circ, 50^\circ$ , and  $35^\circ$  for I/Si, I/Ge, Te/Si, and Te/Ge, respectively.

<sup>c</sup> The relative amplitudes (i.e. the ratios) are determined without reference to the model compound, thereby explaining the smaller experimental uncertainties.

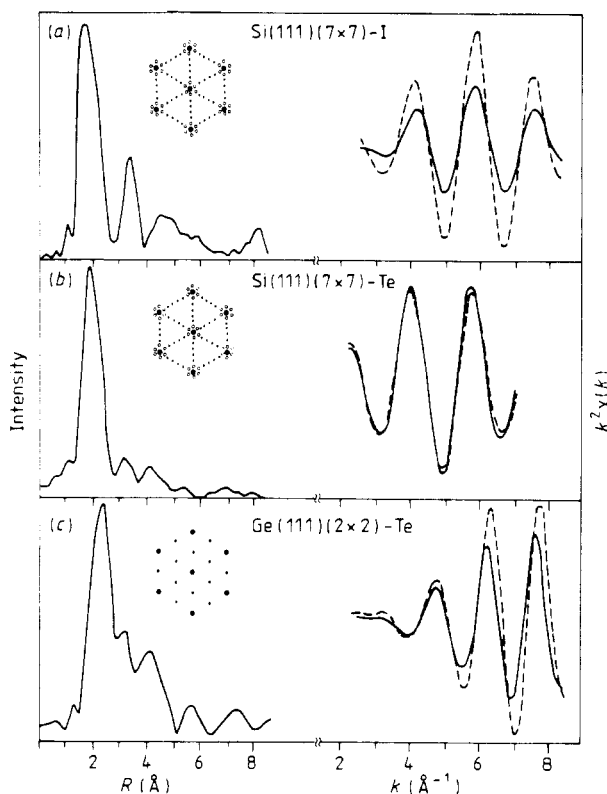


**Figure 9.** FTs of SEXAFS data (left) taken at  $\theta = 90^\circ$ , i.e.  $E$  parallel to surface, with the corresponding LEED patterns. Polarisation-dependent filtered data (right) taken at  $\theta = 90^\circ$  (full curve) and  $\theta = 35^\circ$  (a),  $50^\circ$  (b),  $35^\circ$  (c) (broken curve). Note the differences in amplitude and phase dependence with  $\theta$ .

of the change in anion coordinations in the analogous bulk compounds ( $\text{SiI}_4$  versus  $\text{GeI}_2$  and  $\text{SiTe}_2$  versus  $\text{GeTe}$ ). However, this would suggest a different site for iodine adsorption on the two surfaces, which does not occur. It is immediately obvious from the experimental data (given in figure 9 after Fourier transformation and filtering) that the Te site cannot be the onefold position observed for iodine, since the polarisation dependence of amplitude and phase is completely different. Inspection of both relative and absolute SEXAFS amplitudes easily rules out both the high-symmetry sites 1 and 3 (figure 8) but the unambiguous distinction between sites 2 and 3' requires the use of amplitude *and* distance information: this is readily possible with the high-quality data obtained and leads to the conclusion that site 2 (a twofold bridge site) is occupied for Te on Si(111) but that, on Ge(111), the Te atoms occupy site 3' (the 'HCP' threefold hollow) in alternate rows. Neither of these sites has previously been proposed for a (111) surface so we should consider the implications for bonding on this surface. It is understandable *a posteriori* that divalent Te should favour a twofold bridging site on Si(111), with one electron per dangling bond, and this again fits in with the directional bond saturation arguments advanced earlier. Te on Ge is more complex, and indeed the model suggested does not explain all of the observations relating to longer-range order—the higher-distance structure in the FT data (figure 9) or the  $(2 \times 2)$  symmetry of the annealed

surface—yet it is clear that the threefold hollow site above the substrate atom (3') is the only one of the four possible high-symmetry sites that fits the short-range SEXAFS data. Reconstruction involving several layers of Ge atoms may have to be invoked to explain the long-range structure: such an analysis could well be beyond the capabilities of SEXAFS, which is essentially a short-range phenomenon. Finally it is worth noting that, out of the four high-symmetry sites possible for the (111) surface, three have been identified with Te or I on Si and Ge, and none of them corresponds to the FCC threefold site most commonly observed for adsorption on (111) metal surfaces.

#### 4.3. SEXAFS of a clean surface: amorphised silicon

Since each Auger transition in a particular atom has a characteristic kinetic energy, it also has a characteristic electron mean free path (see figure 3), and thus by measuring different Auger lines from a solid, the surface sensitivity can be altered. Of course, to use this to monitor EXAFS, the intensity of each of the Auger peaks must be proportional to the number of photons absorbed at the initial core level: inspection of figure 1 shows that this is indeed the case since, starting for example from the K edge, photon absorption produces KLL Augers and each KLL Auger electron leaves two L holes, which are then filled by LMM Augers, and so on. The yield of *any* Auger line is thus proportional to the photon absorption coefficient at the initial core level.

This idea has been used to look at the difference between the near-surface and deeper regions on a silicon crystal that had been ion bombarded and thus damaged near to the surface (Comin *et al* 1985). The absorption spectra from single-crystal and evaporated silicon are shown in figure 10. These systems are expected to differ in their medium-range order (MRO), with similar nearest neighbours but distinctly different second- and third-neighbour structure. Fourier transformation of these data (figure 11(a)) indeed shows clear evidence of strong second- and third-shell contributions in the crystalline sample, but only weak structure beyond the first shell in the evaporated (amorphous) Si. These data have been curtailed at only 90 eV above the absorption edge, for later

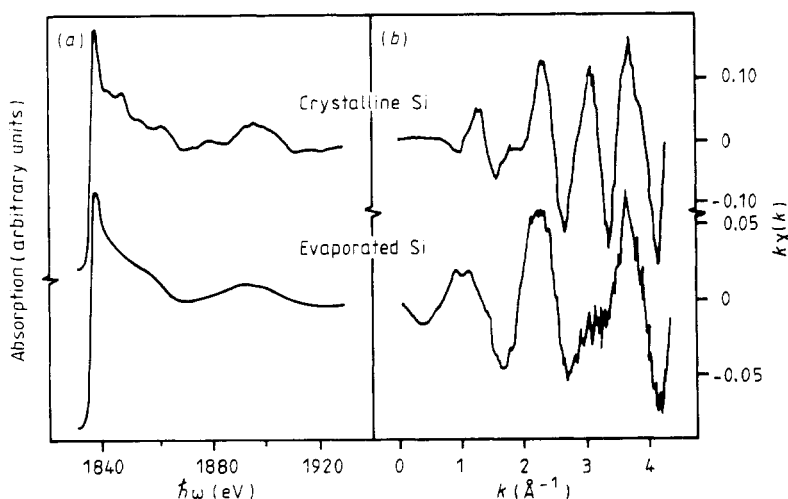


**Figure 10.** (a) K-edge adsorption spectra from single-crystal and evaporated Si measured with Si KLL Auger electrons. (b) The same data after background subtraction and conversion to  $k$ -space.

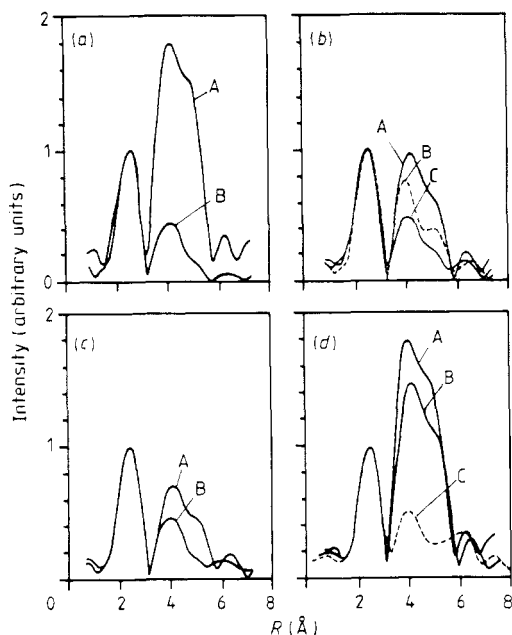


**Figure 11.** FTs of Si K-edge spectra as a function of sample preparation and measurement detection mode. Variations in intensity of the unresolved second- and third-coordination-shell structure at 4–5 Å reflect changes in medium-range order. (a) Single-crystal (A) and evaporated (B) Si measured with KLL Auger electrons (raw data in figure 10). (b) Ne<sup>+</sup>-sputtered (C) and Kr<sup>+</sup>-sputtered (B) (both with KLL Augers) and Ne<sup>+</sup>-sputtered (A) measured with TY (identical to Kr<sup>+</sup> sputtered, TY). (c) Ne<sup>+</sup>-sputtered crystalline Si (A) (raw data in figure 12) and evaporated Si (B) measured with LVV Auger electrons. (d) The FT of the raw difference spectrum for Ne<sup>+</sup>-sputtered crystal (B) (raw data in figure 12), evaporated Si (C) treated with the same data manipulation procedure and KLL-measured single-crystal data (A) (from panel (a)).

comparison with spectra collected with LVV Auger electrons, where direct photo-emission from the Si K level enforces this low limit: thus a single-scattering EXAFS analysis is not valid, and *absolute* values cannot be obtained, but *comparisons* between different samples can still be satisfactorily made. Both of the spectra in figure 10 were measured by detecting Si KLL Auger electrons, at a kinetic energy of 1615 eV. Figure 11(b) shows the FT of data taken by monitoring either the Si KLL Auger yield or the total electron yield (TY) from single-crystal samples that had been amorphised by sputtering with Kr<sup>+</sup> or Ne<sup>+</sup> ions. Since the TY is dominated by low-energy electrons, with quite long MFPS ( $\geq 50$  Å), the TY spectrum contains a substantial contribution from the crystalline region beyond the penetration depth of the sputtering ions, whereas the KLL Auger electrons probe less deeply into the bulk because of their  $\sim 25$  Å escape depth. The KLL spectrum, preferentially probing the amorphised region, therefore shows less evidence of second- and third-shell structure in the FT. The lighter Ne<sup>+</sup> ions have a greater range than the Kr<sup>+</sup>, and the sputter-damaged region is seen to be deeper after Ne<sup>+</sup> bombardment, and this Ne<sup>+</sup>-treated sample appears very similar to the evaporated (amorphous) silicon sample shown in figure 11(a). Thus it is demonstrated that the degree of MRO may be monitored in the FT data, and its variation with depth can be probed with different electron yield detection schemes.

The extension of this method to measure clean silicon surface geometries (Comin *et al* 1985) involves using the difference in escape depth between the Si KLL and LVV Auger electrons: the MFP for the LVV electrons is about 5 Å, making them a factor of five more surface-sensitive than the KLL Augers. The results of measuring the Ne<sup>+</sup>-sputtered Si sample in these two ways are shown in the upper part of figure 12. The more surface-sensitive LVV data exhibit additional structure which the FT data (figure 11(c)) clearly identify as increased MRO. The mean escape depth of the LVV electrons is around three or four atomic layers, so their spectrum includes more than just the topmost surface layer, which can be isolated in the data analysis by taking a *difference* spectrum composed of a linear combination of the LVV and KLL data. This spectrum is shown as the full trace in the lower part of figure 12 and, after Fourier transformation, in figure 11(d), and resembles very closely the KLL spectrum from crystalline silicon (superimposed in the same figures). The inference is clear: the surface layer of the sputtered silicon has recrystallised, and the local structure around the surface silicon atoms is virtually indistinguishable from that of the bulk atoms in a single-crystal sample.

This work again shows the advantage of the short-range-order probe of SEXAFS. Since no long-range periodicity is needed for the measurement, the sample may be analysed in the same way, regardless of whether it is a single crystal, or in a polycrystalline or amorphous state. The significance of this work extends beyond its immediate findings on the surface recrystallisation of a sputtered silicon sample. All other SEXAFS work had achieved its surface specificity by using the atom-specific nature of x-ray absorption to

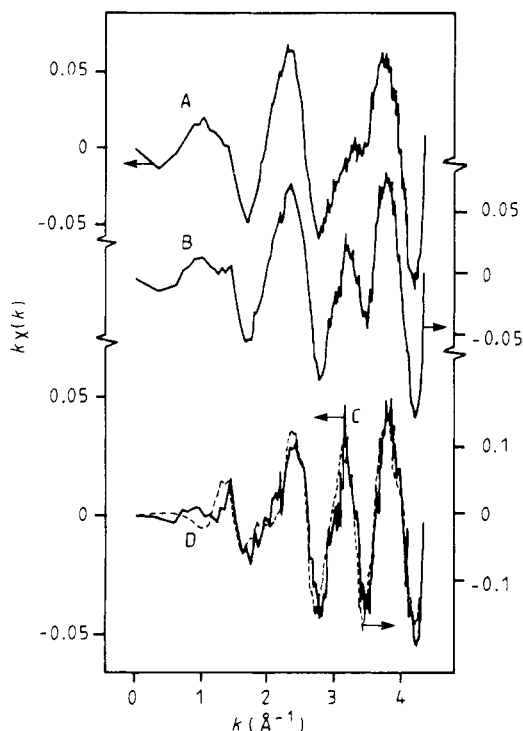


**Figure 12.** Spectra from Ne<sup>+</sup>-sputtered Si measured with KLL (A) or LVV (B) Auger electrons and (C) a difference spectrum (LVV -  $\alpha$ KLL), further enhancing the surface contribution, compared with the single-crystal data (D) from figure 10.

measure foreign adatoms on surfaces. With the use of this depth-selective Auger probe it appears possible to analyse many types of system to determine the difference between surface atoms and the same type of atoms within the bulk of a solid. A short data range is enforced by the relatively low binding energies of the core levels necessarily used to achieve really short MFPS, thus hindering attempts to analyse data with the EXAFS single-scattering formalism, but comparisons between spectra measured in different ways will still be valid, and this extension of the SEXAFS technique appears to be quite widely applicable.

#### 4.4. Ionic-covalent transition in adlayers of electropositive atoms

Adsorption of alkali-metal atoms onto a metal substrate can result in a substantial decrease in the work function as the surface charge distribution becomes dominated by the electropositive atoms. When the alkali-metal coverage is increased, in the sub-monolayer range, the alkali atoms change continuously from an ionic state towards their neutral (covalent) state. Since the effective radius of an atom depends on its charge state, such a change in ionicity might be expected to be accompanied by a change in adsorbate-substrate bond length. This effect has been measured directly by using SEXAFS (Lamble *et al* 1986b).

The SEXAFS results for 0.15 and 0.3 monolayers of Cs adsorbed on Ag(111) are shown in figure 13, which displays just the frequency component corresponding to the Cs-Ag NN distance, extracted from full multi-shell fits to the experimental spectra. These data were analysed not by the Fourier-filtering and phase-shifting methods used above, but by a least-squares curve-fitting procedure (Gurman *et al* 1984). This scheme has been tested on a very wide variety of bulk and surface systems, and gives results equivalent to the other methods. Curve fitting is a superior technique when different shells of neighbours occur sufficiently close in distance to be inseparable by Fourier transformation and windowing, which is the case in this experiment. A fundamental limit on the ability to distinguish shells of neighbours separated by a distance  $\Delta R$  is set by the range of the data, according to  $\Delta R \sim \pi/2k_{\text{max}}$ , where  $k_{\text{max}}$  is the maximum value of wave-

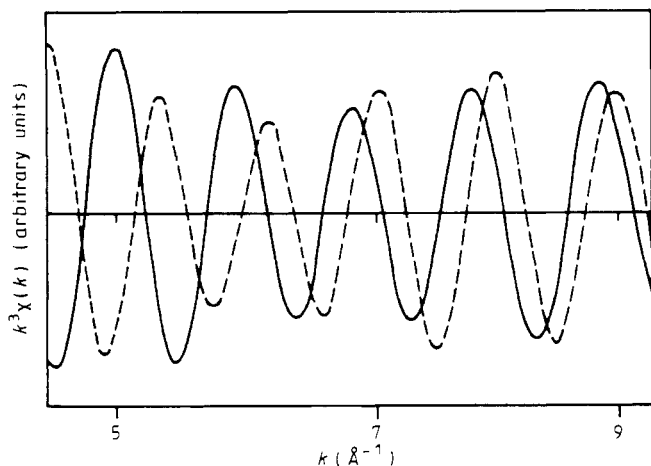


**Figure 13.** Fourier-filtered Cs-Ag nearest-neighbour spectra for 0.15 (full curve, low coverage) and 0.3 (broken curve, high coverage) monolayers of Cs adsorbed on Ag(111).

vector in the spectrum. For surface EXAFS spectra where the data range is often limited (see § 2),  $\Delta R \approx 0.2 \text{ \AA}$ .

Figure 13 shows that there is clearly a coverage-dependence change in the EXAFS frequency, associated with a change in bond length. In analysing the data further, to determine the absolute values of bond lengths, there are two real physical problems that conspire to limit the accuracy obtainable for bond lengths in this system. First, as with most metal-metal adsorption systems, no *perfect* model compound exists, with Cs and Ag bonded to each other, against which scattering phase-shifts may be checked and refined. Although the assumption of phase-shift transferability, discussed earlier, undoubtedly holds good, it is usually desirable to be able to check the transferred phase-shifts directly in a similar compound. In this case phase-shifts were tested indirectly by transferring between CsBr, AgCl, CsCl, AgBr and Ag metal. Second, the atomic back-scattering factor  $f_i(k)$  for Ag contains a Ramsauer-Townsend resonance (see also Citrin *et al* 1978), the effect of which is to produce a modulation of the EXAFS amplitude as a function of wave-vector. This then gives an additional frequency component corresponding to an apparent peak at a shorter distance. In the Cs-Ag system this 'split-off' peak due to the Ag back-scattering resonance in the *second* NN silver shell actually occurs at a similar distance to the main peak for the first NN Ag shell. It is possible to deal with this in a multi-shell fitting procedure, but inevitably this overlap somewhat diminishes the accuracy of determination of the Cs-Ag distance. The detailed analysis then gives the NN Cs-Ag distance as  $3.20 \text{ \AA}$  for the lower-coverage phase (0.15 monolayers of Cs) and  $3.50 \text{ \AA}$  for the higher coverage of 0.3 monolayers of Cs: note that this high-coverage phase is close to a full close-packed overlayer of the large caesium atoms, with coverages expressed in terms of the silver surface atoms. With all random and systematic errors included, a change in NN distance of  $0.3 \pm 0.06 \text{ \AA}$  is quoted between the two phases.

No change is expected in the effective radius of the silver, since the bulk atoms are well screened, and the coverage-dependent change in adsorbate-substrate bond length is attributed to an increase in the caesium effective radius as it goes from a largely ionic towards a more covalent state. This change in bond length as a function of Cs coverage contrasts with studies of chlorine adsorption on the same Ag(111) surface, where an identical Cl-Ag NN distance is seen at different Cl coverages (Lamble *et al* 1986a). The reason for this difference in behaviour is postulated to be related to the change in potential induced at the surface by the adatom. Around an adsorbed chlorine atom, the total charge distribution one lattice vector away, along the surface, is little different from that of the clean metal and thus another chlorine atom may be adsorbed in a site with a NN substrate distance the same as that of the first Cl atom. However, the situation is dramatically different for adsorption of Cs atoms: the charge distribution on the surface near to an adsorbed Cs atom is considerably different from the potential of the clean metal surface. This is another way of expressing the fact that a relatively low coverage of alkali-metal atoms gives a marked reduction in the metal work function. Thus the adsorption of further Cs atoms near to one already on the surface will not be at the same adsorbate-substrate distance. Presumably the detailed energy balance will lead to an equilibrium distribution of atoms at a particular adsorbate-substrate distance rather than a spread of dissimilar NN distances.

The importance of this application of SEXAFS is in demonstrating a coverage-dependent adatom-substrate bond length in a range of coverages where no long-range order exists in the overlayer. No other technique is available that can do this, and SEXAFS is ideal since it can probe directly the structural environment around an adsorbate atom.



There is a large amount of information available on the effects of local charge distribution on bulk chemical and crystallographic properties (Pauling 1960): for the analogous surface properties, however, there is no such expansive body of data. The use of SEXAFS has the promise to help remedy this.

## 5. Near-edge studies

### 5.1. XANES of an atomic adsorbate: oxygen on nickel

The XANES region near to the absorption edge is usually discarded in an EXAFS analysis because the strong scattering and longer MFP of the excited photo-electron give rise to sizable multiple-scattering corrections. It is this region, however, that exhibits the largest modulations of the atomic absorption coefficient and is therefore the most easily recorded experimentally. The first experimental and theoretical XANES study of a chemisorption complex dealt with oxygen on a single-crystal Ni(100) surface (Norman *et al* 1983).

Increasing exposures of oxygen on a Ni(100) surface give consecutive formation of a  $p(2 \times 2)$ , a  $c(2 \times 2)$  and a  $\text{NiO}(1 \times 1)$  LEED pattern. The XANES spectra measured above the O K absorption edge for increasing oxygen exposures are shown in figure 14 for two different angles of incidence of the photon beam. The spectra for low oxygen exposures show a very pronounced polarisation dependence which weakens at higher oxygen coverages. For 280 L exposure (not shown) the XANES spectrum looks identical to that in figure 14(h) for both angles of incidence. It has become completely isotropic and is the same as that for FCC bulk NiO, there being no polarisation dependence in a

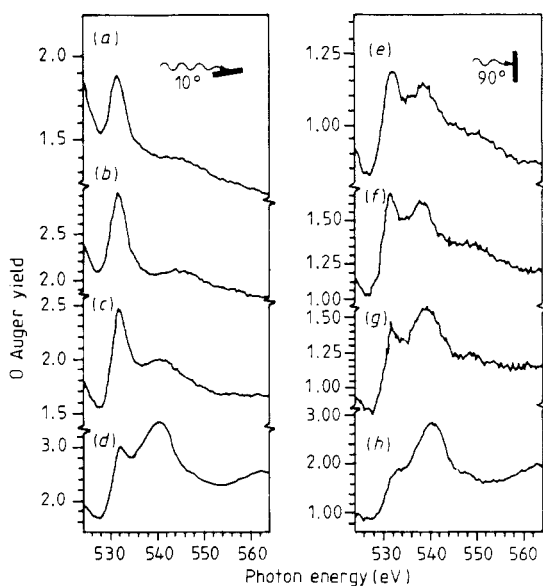


**Figure 14.** X-ray absorption near-edge structure above the O K edge for increasing oxygen coverage on Ni(100), measured at two different photon incidence angles. The strong polarisation dependence (at low coverage) tends to disappear at high coverage due to formation of cubic NiO: (a),  $p(2 \times 2)$ , 1.5 L; (b),  $c(2 \times 2)$ , 10 L; (c), 80 L; (d), 160 L; (e)–(h), as (a)–(d) respectively.

cubic system. Note that the grazing-incidence 160 L spectrum (figure 14(d)) slightly differs from that for bulk NiO because it preferentially probes the thin ( $<3$  layers) oxide film perpendicular to the surface. Since the edge fine structure is more easily recorded (collection time of about 10 min) than a complete SEXAFS spectrum ( $>2$  h) figure 14 represents a good example of how an unknown system might be characterised first by XANES before addressing certain structural issues by SEXAFS. Furthermore, it was demonstrated (Norman *et al* 1983) that the near-edge spectrum could itself yield detailed structural information when compared with an appropriate calculation.

The XANES calculations were performed using the computational scheme of Durham *et al* (1982), which is based on a cluster method and includes full multiple scattering. The calculations included around 30 atoms to a distance  $>5.0$  Å from the central O atom, this number being found necessary to produce full convergence. The O–Ni distance is known (1.98 Å, Stöhr *et al* 1982) and XANES calculations were performed, with this bond length constraint, for different high-symmetry chemisorption sites. Figure 15 compares the polarisation-dependent experimental data for a  $c(2 \times 2)$  O overlayer on Ni(100) with the results of the calculations. For the hollow site with  $d_{\perp} = 0.9$  Å the peaks in the calculated spectra appear at energies within about 2 eV of the experimental ones and the relative peak intensities are also in good agreement. The fit is considerably worse for all the other sites considered, and in particular  $d_{\perp} = 0.2$  Å in the fourfold hollow site, which had been suggested from some other studies (Upton and Goddard 1981), does not give agreement with the experimental spectra.

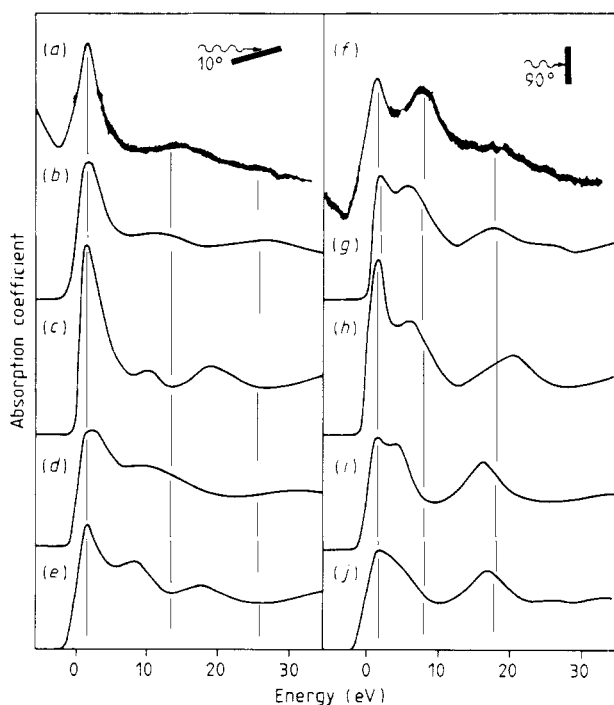


**Figure 15.** Experimental and calculated XANES for  $c(2 \times 2)$ O on Ni(100). The calculated spectra included full multiple scattering and assumed different chemisorption sites as indicated: (a),  $c(2 \times 2)$ , experiment; (b), hollow,  $d_{\perp} = 0.9$  Å; (c), hollow,  $d_{\perp} = 0.2$  Å; (d), bridge; (e), atop; (f)–(j), as (a)–(e) respectively.

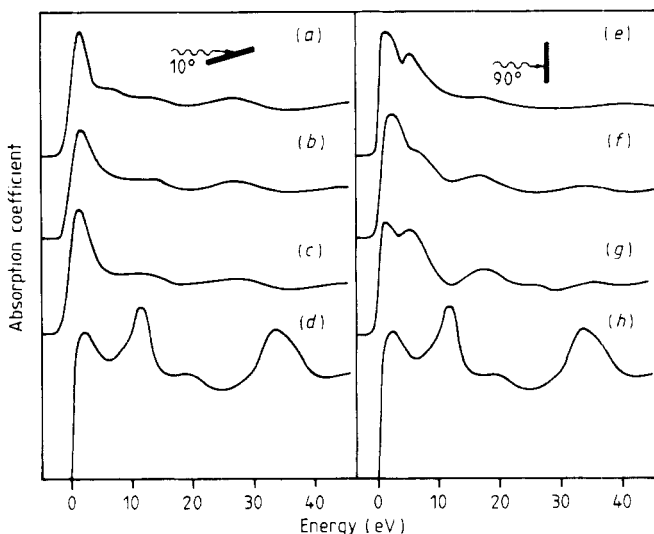


**Figure 16.** Calculated polarisation-dependent O K XANES for increasing oxygen coverage on Ni(100). Changes in the top three spectra are due to scattering off additional O neighbour atoms. The lowest spectra are for bulk NiO, which shows no polarisation dependence: (a), isolated atom; (b),  $p(2 \times 2)$ ; (c),  $c(2 \times 2)$ ; (d), NiO; (e)–(h) as for (a)–(d) respectively.

Figure 16 shows the effect of adding oxygen atoms around a central O atom in the fourfold hollow site with  $d_{\perp} = 0.9 \text{ \AA}$  to give a  $p(2 \times 2)$  and  $c(2 \times 2)$  surface net. For comparison the XANES calculation for FCC NiO is also shown. It is seen from the upper three spectra that scattering off the other adsorbate atoms is non-negligible, especially when the electric field vector lies in the surface plane (normal incidence). The difference between the  $p(2 \times 2)$  and  $c(2 \times 2)$  calculations is, however, small. The NiO calculation is seen to be in good agreement with spectrum (h) in figure 14.

These results show that the polarisation-dependent XANES provides a sensitive tool to monitor structural changes at surfaces. It is possible to model the data by a multiple-scattering calculation and in fact discriminate between some different structural possibilities. The use of XANES to obtain structural information for atomic adsorption on solid surfaces is thus shown to be possible. There are two advantages with respect to SEXAFS. XANES measurements can be performed for lower adsorbate coverages (maybe 1/100 monolayer) and they can be carried out even if absorption edges occur too close together to allow a SEXAFS analysis. However, if this O/Ni result is generally true, from a practical point of view it must be considered a major disappointment that the XANES spectra of *atomic* adsorbates are not dominated by just the NN substrate atoms, but rather that the scattering from as many as 30 neighbour atoms has to be included in the calculation before convergence is achieved. This is in contrast to the near-edge structure of *molecular* adsorbates, considered in the next few sections, where the spectra are dominated by intra-molecular scattering with only small or negligible scattering contributions from the surface substrate atoms.

## 5.2. Molecular orientation from XANES (NEXAFS)

The adsorption of carbon monoxide on metals, particularly nickel, is probably the most

studied system in surface science. CO adsorbs molecularly—although intense electron beams or elevated temperatures may crack the molecule—and it is of interest to determine the orientation of the intact molecule on the surface. This has in fact been deduced from a comparison of photo-emission measurements (Allyn *et al* 1977) with oriented molecule calculations (Davenport 1976), but the use of polarisation-dependent x-ray absorption for this purpose is particularly direct and instructive, and leads on to studies of other, more complicated, chemisorption systems.

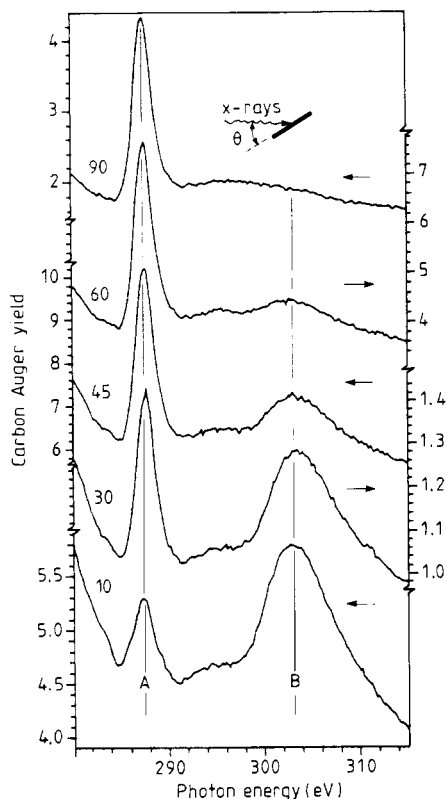


**Figure 17.** Near-edge x-ray absorption fine structure (NEXAFS) above the C K edge for a saturation coverage of CO on Ni(100) measured at  $T = 180$  K and a variety of photon incident angles (given by traces in degrees).

Figure 17 shows the absorption spectra near the C K edge (NEXAFS) for a saturation coverage of CO on Ni(100), measured at different angles to the photon beam (Stöhr *et al* 1981, Stöhr and Jaeger 1982). At normal incidence ( $\theta = 90^\circ$ ), with the  $E$ -vector parallel to the sample surface, a large peak (A) at 287.5 eV dominates the spectrum. As the angle  $\theta$  is reduced, and  $E$  rotates towards the surface normal, peak A loses intensity and peak B emerges at around  $h\nu = 303.5$  eV. Spectra recorded above the O K edge show the same features and polarisation dependence. Peak B is assigned to a transition from the C 1s state to a resonance of  $\sigma$ -symmetry in the continuum, a so-called 'shape resonance' (Dehmer and Dill 1975). The molecular  $\sigma$ -orbitals, arising from the 2s and  $2p_z$  atomic orbitals of the C and O, are symmetric, oriented along the molecular axis.

The transition involved in peak B is to the unfilled, anti-bonding part of the  $\sigma$ -orbital. The shape resonance is caused by a high potential barrier to the escape of the excited photo-electron, due to centrifugal barriers in higher-angular-momentum states, leading to the electron's becoming trapped in this quasi-bound anti-bonding state which thus has enhanced amplitude on the molecule. A  $\sigma$  shape resonance in CO adsorbed on Ni has been observed in photo-emission studies (Allyn *et al* 1977). Peak A in figure 17 is identified as a  $\pi$ -resonance, arising from transitions from the C 1s state to the unfilled  $\pi^*$  bound state (anti-symmetric) molecular orbital. Since this peak lies below the continuum K-shell ionisation threshold, it cannot be seen by photo-emission.

The variation of cross section of these resonances with polarisation angle gives the molecular orientation. The transitions are governed by dipole selection rules so, with linearly polarised light and an oriented molecule with cylindrical symmetry (Wallace and Dill 1978),

$$\mu(\psi) \propto 1 + (\beta/2)(3 \cos^2 \psi - 1)$$

where  $\psi$  is the angle between the  $E$ -vector and the intra-molecular symmetry axis and  $\beta$  is the well known asymmetry parameter of molecular physics.  $\beta = 2$  for initial s and final  $\sigma$ -states, and  $\beta = -1$  for transitions from s to  $\pi$ -states, giving the simple forms  $\mu_\sigma \sim \cos^2 \psi$  and  $\mu_\pi \sim \sin^2 \psi$ . These equations are analogous to equation (2) above for the EXAFS amplitude. Thus a  $\pi$ -resonance has maximum amplitude when the polarisation vector  $E$  is perpendicular to the intra-molecular bond and zero intensity when  $E$  lies parallel to this axis: the  $\sigma$  shape resonance has the opposite behaviour, being zero when  $E$  is perpendicular to the inter-atomic axis and a maximum if  $E$  lies along this bond.

It is then easy to see from figure 17 that the CO molecule stands upright on the Ni(100) surface. However, this experiment alone tells us only the orientation with respect to the top plane of nickel atoms, not the detailed arrangement of the bonding to the individual surface atoms; nor does it indicate which end of the molecule is next to the surface. These facts may be determined from SEXAFS measurements on the carbon or oxygen atoms. There may be deviations from the perfect angular dependence given above due to non-linear polarisation components of the light or to a tilted molecular axis. These effects may be investigated by a detailed analysis of the intensities of the  $\pi$ - or  $\sigma$ -resonances as a function of polarisation angle. Determination of the area under the  $\pi$ -state peak is usually straightforward. Because of its energy position near to the threshold it is not modified by any underlying absorption structure resulting from transitions to continuum states (including EXAFS structure): this problem can apply to the  $\sigma$  shape resonance, lying farther above the absorption edge. The CO data have been analysed (Stöhr *et al* 1981) to indicate a maximum deviation of the molecular axis from the sample normal of  $10^\circ$ , which is of the same order as the vibrational amplitude. An upright CO molecule had been found in previous studies using other techniques, which may be considerably less straightforward to interpret, but it had similarly been proposed that the NO molecule was tilted on a variety of substrates. X-ray absorption measurements for a saturation coverage of NO on Ni(100) (Stöhr *et al* 1981) gave results identical to the CO: the NEXAFS above the N and O K edge indicates conclusively that the molecule stands upright. It has been suggested that molecular tilting may reduce inter-molecular repulsion, and it is therefore possible that the orientation might depend on the coverage.

The above discussion has virtually ignored the nickel, except inasmuch as it orients the chemisorbed molecule, yet clearly there must be some scattering involving the substrate. The extent of this has been examined in some calculations (Norman and

Durham 1983), where it was shown that the effects of the addition of the correct nickel NN atoms to an isolated, oriented, CO molecule are indeed of minor significance compared with the intra-molecular scattering. Furthermore, only one nickel atom, the one directly bonded to the C atom, had any effect at all. This contrasts greatly with the atomic adsorption of oxygen, described above, where as many as 30 substrate atoms contributed significantly to the XANES. This comparison indicates the magnitude and overwhelming importance of the *intra-molecular* scattering events in molecular chemisorption.

### 5.3. Intra-molecular bond lengths from NEXAFS

Since the shape resonance has  $\sigma$ -symmetry and is largely oriented along the inter-nuclear axis between atoms within a molecule, it might be anticipated that its energy position would bear a direct correspondence to the intra-molecular bond length. Such a relationship has been justified on theoretical grounds (Natoli 1982), demonstrated by multiple-scattering calculations (Norman and Durham 1983), and empirically established for gas-phase (Sette *et al* 1984) and chemisorbed (Stöhr *et al* 1984c) diatomic molecules containing low- $Z$  atoms. (In this context hydrogen atoms may be ignored, since scattering from them is very weak, and so molecules such as acetylene ( $C_2H_2$ ), hydrogen cyanide (HCN) and methylamine ( $CH_3NH_2$ ) all are considered as pseudo-diatomic, although it should be noted that shape resonances involving the bond between hydrogen and heavier atoms may be seen as minor spectral features.) Since the electron scattering is in momentum space we would expect the position of the  $\sigma$ -resonance above threshold to be inversely correlated with the intra-molecular bond length, with a long bond giving a shape resonance close to threshold and a shorter bond showing a peak at higher energy.

The effect is nicely demonstrated in figure 18, which shows the NEXAFS above the O K edge (Stöhr *et al* 1983) for three molecules with carbon-oxygen bonds, chemisorbed on Cu(100). In each case the angle of the  $E$ -vector to the surface has been chosen to maximise the intensity of the  $\sigma$  shape resonance. The three molecular species are CO, with a short (1.13 Å) triple C-O bond, formate ( $HCO_2$ ), with a quasi-double C-O bond, and methoxy ( $CH_3O$ ), whose single C-O bond is long (1.43 Å). Close to the K-edge threshold, which coincides with the O 1s binding energy as determined by photo-emission (marked 'XPS'), a  $\pi$ -resonance peak is seen for CO and formate, corresponding to transitions from the O 1s state into the partially unoccupied anti-bonding  $\pi^*$  orbital in these molecules. Note that the  $\pi$ -peak is minimised for CO with the depicted experimental geometry, as for the CO on Ni(100). There is no such peak for methoxy, since there is no  $\pi$ -character in the single C-O bond. It is clear that care is needed in the interpretation of these spectra, since the structure marked X in figure 18, which is the atomic-like absorption step at the O K edge, could be confused with a weak  $\pi$ -peak, and the small peak around 555 eV, which is an EXAFS 'wiggle' due to O-Cu scattering, must be differentiated from the true shape resonance. Other effects may also intrude upon the near-edge spectrum, such as multi-electron (shake-up) excitations and transitions to atomic Rydberg states (which are often quenched in the solid state), but the molecular resonances can usually be identified by their larger intensity and/or width.

A  $\sigma$  shape resonance is seen for all three molecules, as marked in figure 18, and its position does indeed decrease in energy with increasing C-O bond length. Qualitatively this may be understood in a molecular orbital picture: as the distance increases, the interaction between orbitals on adjacent atoms decreases (i.e. the overlap integrals decrease) and the splitting between bonding and anti-bonding states is reduced. This

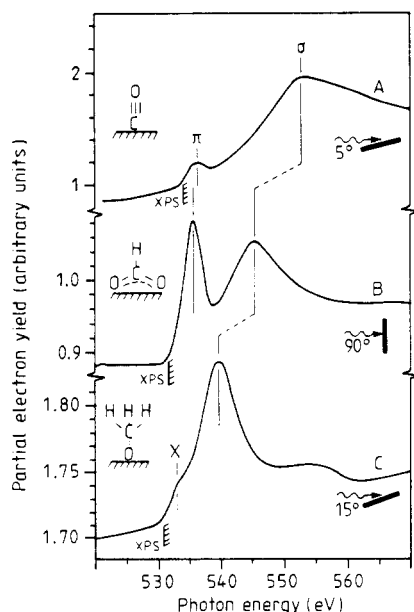


**Figure 18.** NEXAFS spectra of the O K-edge region for CO (A), formate ( $\text{HCO}_2$ ) (B) and methoxy ( $\text{CH}_3\text{O}$ ) (C) on Cu(100). The polarisation is altered to maximise the  $\sigma$ -peak intensity. The O 1s binding energies determined by photo-emission are labelled 'XPS'.

decrease is much greater for orbitals directed along the bond ( $\sigma$ ) than for those perpendicular to it ( $\pi$ ), and the energy position of  $\pi^*$ -resonances is rather little affected by the bond length. A quantitative relationship may be derived for the  $\sigma$  shape resonance position, following Natoli (1982). For scattering between two atoms separated by a distance  $R$  the scattering maximum will be expected to occur at a photo-electron wave-vector  $k_r$ , according to an EXAFS-like expression

$$k_r R = \text{constant}. \quad (6)$$

The constant will be determined by the details of the atomic scattering phase shifts  $\varphi(k)$ , and should therefore be the same for all processes involving scattering between the same pairs of atoms. Also, because of the small energy range, it is reasonable to ignore the  $k$ -dependence of  $\varphi(k)$ , and thus the constant in equation (6) will be identical for all similar molecules. The photo-electron wave-vector  $k_r$  is referred to the approximately constant potential in the interstitial region between the ion cores (the 'muffin-tin zero') and so equation (6) may be rewritten as

$$(\Delta - V_0) R^2 = C_0 \quad (7)$$

where  $\Delta$  is the energy separation of the  $\sigma$  shape resonance from threshold and  $V_0$  is the inner potential between the muffin-tin zero and the Fermi level.  $V_0$  is likely to vary little for different chemisorbed molecules on the same substrate and so, working from the two extreme cases CO and methoxy on Cu(100),  $V_0$  and  $C_0$  may be determined. Thus the  $\sigma$  shape resonance energy in formate chemisorbed on Cu(100) is deduced to correspond to an intra-molecular C–O distance  $R = 1.25 \text{ \AA}$ . This is in excellent agreement with the value  $R = 1.25 \pm 0.02 \text{ \AA}$  for the C–O bond length in formate ions coordinated by a variety of metals, but is somewhat longer than the distance ( $R = 1.21 \text{ \AA}$ ) in gas-

phase  $\text{H}_2\text{CO}$ . This may be the result of stronger interaction of the O atoms with the substrate in the pseudo-bridge bonding to the surface (Stöhr *et al* 1983) but the apparent increase in distance is within the possible error in this method. Evaluation of probable errors led Stöhr and co-workers (1983) to suggest that, with the above procedure, intra-molecular chemisorption bond lengths could be determined to an accuracy of  $\pm 0.05 \text{ \AA}$ , which is comparable with, or smaller than, that obtained with any other surface technique.

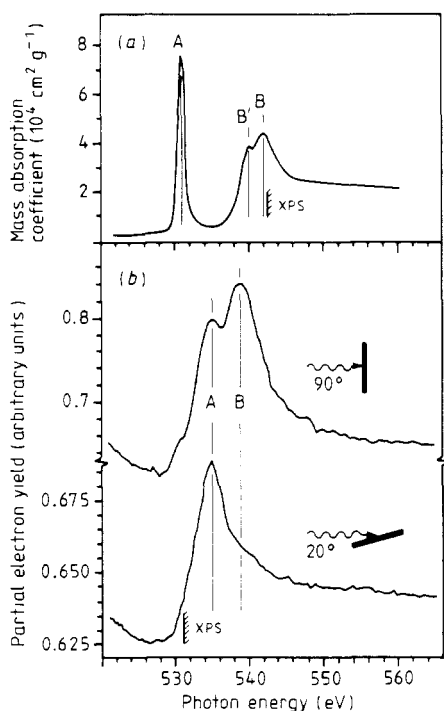


**Figure 19.** Oxygen K-edge NEXAFS for: (a), gas-phase  $\text{O}_2$  (Barrus *et al*) and (b),  $\text{O}_2/\text{Pt}(111)$  at 90 K measured at two different photon incidence angles. Peaks A and B are final-state  $\pi$ - and  $\sigma$ -resonances, peak B' is a multi-electron feature. The O 1s binding energies relative to the vacuum level (gas) and Fermi level (surface) are denoted 'xps'.

The use of NEXAFS to determine bond length changes in a molecule on chemisorption is illustrated in figure 19, which shows a comparison (Stöhr *et al* 1983) between the oxygen K-edge spectrum for  $\text{O}_2$  adsorbed on Pt(111) and for gas-phase  $\text{O}_2$  (Barrus *et al* 1979). Peak A is readily identified to be the final-state  $\pi$ -resonance and peak B is the  $\sigma$  shape resonance. (B' in the gas-phase spectrum is attributed to a multi-electron feature.) The dependence of the surface spectra on x-ray incidence angle unambiguously establishes that the  $\text{O}_2$  molecule lies down on the surface. The dramatic decrease of the separation of peaks A and B (from 11 eV in the gas phase to 4 eV when adsorbed on the surface) indicates a substantial increase of the O–O bond length for chemisorbed  $\text{O}_2$ . The extent of this increase can be quantified by use of equation (7), and using the same muffin-tin constant,  $V_0$ , and phase-shift constant,  $C_0$ , as for the C–O-containing molecules on Cu. This can be justified because (for  $C_0$ ) the scattering phase shifts for



carbon and oxygen are very similar, and (for  $V_0$ ) it has been found empirically that the inner potential changes little for different low- $Z$  molecules adsorbed on various d band metals. This procedure then leads to a distance of  $R = 1.45 \text{ \AA}$  for the O–O bond length in chemisorbed  $\text{O}_2$  on Pt(111), an increase of  $0.24 \text{ \AA}$  from the gas-phase value of  $1.21 \text{ \AA}$ . The large  $\text{O}_2$  bond length on the surface is close to the O–O single bond length in peroxide ( $\text{H}_2\text{O}_2$ ) or in the  $(\text{O}_2)^{2-}$  ion, which is explained by postulating  $\pi$ -bonding of  $\text{O}_2$  on Pt(111) with substantial charge transfer from the metal into the two anti-bonding  $\pi^*$ -orbitals of  $\text{O}_2$ , leaving the molecule in a peroxy-like  $(\text{O}_2)^{2-}$  state. This charge transfer cannot be complete since the presence of a  $\pi$ -resonance shows that there are at least partially empty  $\pi^*$ -orbitals.

It thus seems clear that, based on empirical investigations, a correspondence exists between the intra-molecular bond length and the energy position of K-shell shape resonances in many molecules containing B, C, N, O and F (Sette *et al* 1984). However, some gas-phase molecules (e.g.  $\text{CO}_2$ ,  $\text{N}_2\text{O}$  and  $\text{NO}_2$ ) do not fit the general observations. This may be in part because multiple-scattering interference effects come into play in linear molecules (like  $\text{CO}_2$  and  $\text{N}_2\text{O}$ ), and in part because the molecular orbitals are spread out over all three atoms and the concept of resonant enhancement by the shape of the potential along a particular inter-atomic axis is then lost. The whole idea of *any* general relationship between shape resonance position and intra-molecular bond length has also been questioned (Piancastelli *et al* 1985). However, there seems to be sufficient phenomenological evidence to allow such interpretations provided that care is exercised in the peak assignments.

#### 5.4. Orientation and reaction chemistry of polyatomic molecules

The arguments developed in the previous section about the polarisation dependence of  $\pi$ - and  $\sigma$ -resonances can also be applied to more complex molecular adsorbates. Here I discuss the determination of the orientation of benzene ( $\text{C}_6\text{H}_6$ ), pyridine ( $\text{C}_5\text{H}_5\text{N}$ ) and thiophene ( $\text{C}_4\text{H}_4\text{S}$ ), and the thermal decomposition of thiophene, on Pt(111) surfaces (Johnson *et al* 1983, Stöhr *et al* 1984a).

The NEXAFS for the C K edge of benzene is shown in figure 20, which depicts spectra from the gas-phase molecule (measured in a 'pseudo-photon' experiment with inner-shell EELS), from a solid multi-layer, and from one monolayer coverage on Pt(111), taken at two different angles of photon incidence. Peaks A and B are attributed to  $\pi^*$ -resonances (of  $e_{2u}$  and  $b_{2g}$  symmetry) and peaks C and D are due to C 1s  $\rightarrow \sigma^*$  shape resonances. The polarisation dependence of the main  $\pi$ -peak (A) alone immediately indicates that the benzene molecule lies down on the surface, with its  $\pi$ -orbitals projecting along the surface normal, perpendicular to the plane of the benzene ring. A comparison of the spectrum with those of gas-phase and solid benzene (Horsley *et al* 1985) shows less than 1 eV change in the positions of peaks C and D upon chemisorption, implying, since these  $\sigma$ -resonances are known to be sensitive to intra-molecular geometry, that there is at most a  $0.02 \text{ \AA}$  change in C–C bond length.

The spectra for pyridine are shown in figure 21, where the peak assignments are the same as for benzene. The opposite polarisation dependence shows that the pyridine molecule stands up on the surface, with its ring in a plane near to the surface normal. Peak A is narrower than for benzene, showing that in the case of benzene it is probably broadened by hybridisation in bonding to the surface, but suffers no such broadening when the  $\pi$ -orbitals are not involved in bonding to the surface, as in pyridine. The

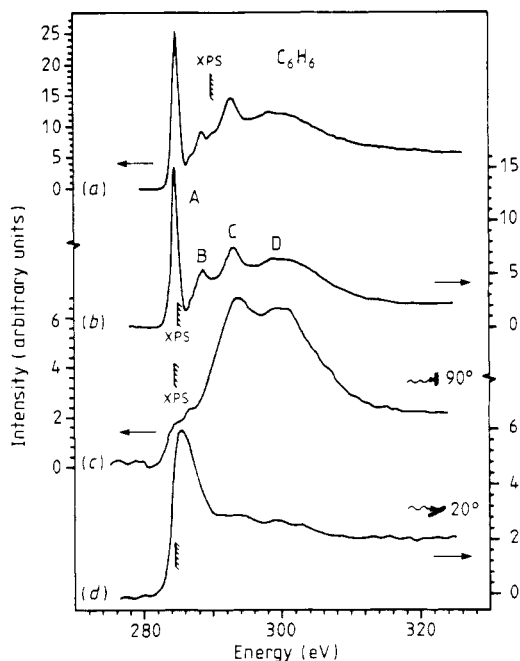


**Figure 20.** The C K-edge NEXAFS in various samples of benzene: (a) gaseous benzene (measured by electron energy-loss spectroscopy), (b) solid benzene, a multi-layer condensed on Pt(111) at  $T = 100$  K, (c) and (d) a monolayer of benzene chemisorbed on Pt(111), at two different polarisation angles at  $T = 200$  K. Peaks A and B are assigned to  $\pi$ -resonances and peaks C and D to  $\sigma$  shape resonances.

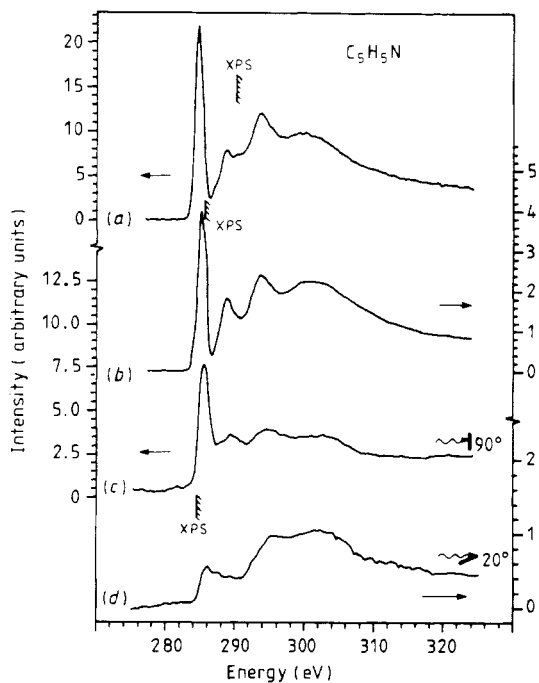


**Figure 21.** C K-edge NEXAFS spectra for pyridine, equivalent to figure 20, except (c) and (d) measured at  $T = 300$  K.

pyridine molecule is indicated to bond to the surface through the nitrogen lone-pair orbitals. The opposite orientation of these two similar molecules is thus easily established by comparison of their C K-edge NEXAFS spectra.

Figure 22 shows the equivalent spectra for a compressed layer of thiophene ( $C_4H_4S$ ), also on a Pt(111) surface (Stöhr *et al* 1984a). These measurements were taken at a temperature of 90 K after the sample had been heated to 150 and 180 K, as indicated. Peak A, as before, is due to transitions from the C 1s level into the anti-bonding  $\pi^*$ -orbitals of thiophene. Peaks C and D are attributed to shape resonances associated with

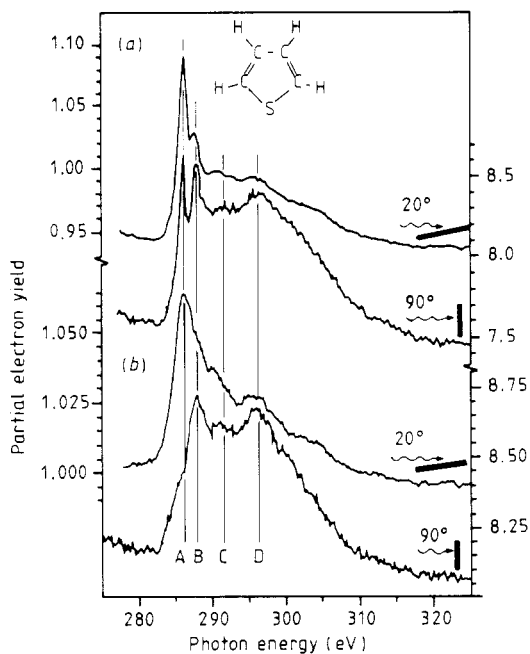


**Figure 22.** C K edge polarisation-dependent NEXAFS spectra for thiophene ( $C_4H_4S$ ) on Pt(111), measured at  $T = 90$  K: (a) after annealing to  $T = 150$  K, giving a compressed layer of thiophene, and (b) after annealing to  $T = 180$  K, corresponding to monolayer coverage. Peak B is a  $\sigma$  shape resonance associated with the C–S bond. Peak A is a  $\pi$ -resonance, which becomes broader and exhibits a stronger polarisation dependence after annealing to  $T = 180$  K.

C–C bonds in the thiophene molecule. Peak B, which is absent in all NEXAFS of pure hydrocarbons, is assigned to a  $\sigma$  shape resonance due to the C–S bonds. Using the dipole selection rules and the polarisation-dependent spectra, as before, indicates that the  $C_4H_4S$  at 150 K is oriented with the ring plane tilted by about  $40^\circ$  from the surface. After annealing to 180 K, which desorbs some of the thiophene to leave a coverage of one monolayer, figure 22(b) shows a much more pronounced polarisation dependence and a considerably broadened  $\pi$ -resonance peak, indicative of a molecule lying down on the surface and bonding to the metal through its  $\pi$ -orbitals, as shown above for benzene.

Peak B is also seen to be broadened, suggesting that the Pt surface also interacts with  $\sigma^*$ -orbitals near the S end of the molecule.

The thermal decomposition of the thiophene molecule on the Pt(111) surface has also been investigated in the same work (Stöhr *et al* 1984a), in conjunction with thermal desorption, XPS and EELS measurements, and figure 23 shows the NEXAFS spectra at the C K edge and the S  $L_{2,3}$  edge (the spin-orbit splitting being unresolved) as a function of increasing anneal temperatures. Peak X is a resonance characteristic of the C-S bond, corresponding to transitions of S 2p electrons into closely spaced unfilled  $\pi^*$  and  $\sigma^*$  molecular orbitals associated with the S-C bond in thiophene. Peak Y is an atomic S resonance due to excitations to d-like final states in the continuum. With increasing anneal temperatures, peak X decreases in intensity, having vanished by 470 K, while peak Y shows the opposite behaviour. This indicates the thermal breaking of the molecular C-S bonds, which occurs to some extent at 290 K and is complete by 470 K. The C K edge NEXAFS spectra shown in figure 23(b) support this conclusion: peak B, due to the C-S bond, follows the intensity change of peak X in figure 23(a). Peak A increases in intensity but is shifted by 0.5 eV to lower energy from the  $\pi^*$ -resonance in thiophene at low temperatures (figure 22). This is attributed to the formation of a molecular species with a similar carbon skeleton to thiophene, slightly inclined to the surface, and incorporating a C-Pt bond.

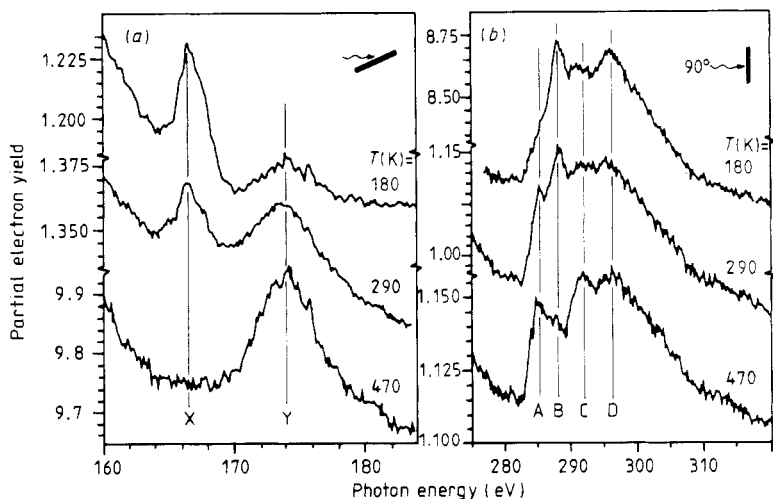


**Figure 23.** NEXAFS spectra at (a) the S  $L_{2,3}$  edge and (b) the C K edge for thiophene ( $C_4H_4S$ ) on Pt(111) after annealing to different temperatures. Peak X represents a resonance associated with the C-S bond, like peak B; note that they disappear after higher-temperature anneals.

More information has been gained on the C-S bond-breaking mechanism from SEXAFS and NEXAFS measurements on thiophene adsorption on Ni(100) (Stöhr *et al* 1985). These experiments were performed by monitoring the S K-fluorescence yield: by this means very high sensitivity was achieved, making possible detection of as little as

one monolayer of thiophene, which is equivalent to about 0.08 monolayers of sulphur. Figure 24 shows the S K-edge NEXAFS spectra (measured at 100 K) after exposures of the Ni(100) surface to 1 and 12 L of thiophene, and also after heating the higher-coverage sample to room temperature. The left-hand panel of figure 24 refers to thiophene exposures on a clean nickel surface, and the right-hand panel shows adsorption on a Ni(100) surface which had been pre-dosed with oxygen to form the  $c(2 \times 2)$  overlayer pattern, filling half of the fourfold hollow sites as discussed in § 5.1 above. Peak B is the

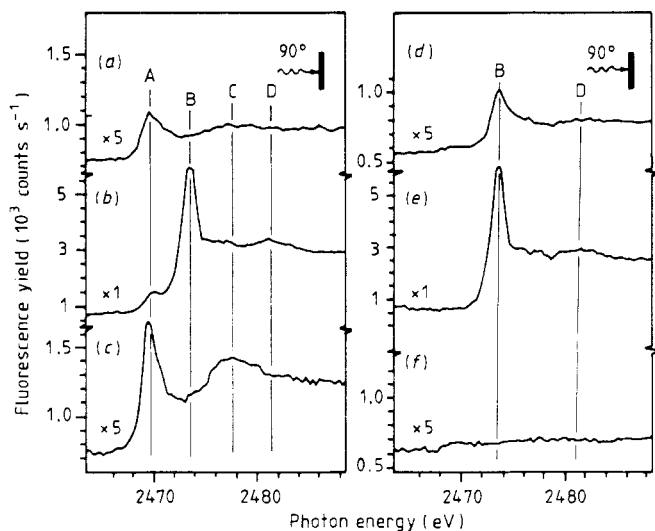


**Figure 24.** S K-edge NEXAFS spectra, measured by fluorescence yield, for thiophene adsorbed on clean (a)–(c) and oxygen-pre-dosed (d)–(f) Ni(100) at various exposures and temperatures. (a), 1 L exposure at 100 K; (b), 12 L exposure at 100 K; (c), sample in (b) heated to 270 K; (d)–(f), are equivalent to (a)–(c), taken after thiophene adsorption on the  $c(2 \times 2)$  O-covered surface. Peaks A and C are characteristic of atomic sulphur on nickel and peak B is associated with the C–S bond.

resonance characteristic of the C–S bond, analogous to peak B at the C K edge in figure 23(b), whereas peaks A and C are associated with S–Ni bonds and are seen for atomic sulphur adsorption on Ni(100). The occurrence of peak A, and the absence of peak B, for the lowest thiophene exposure on the clean surface shows that the C–S bond is broken by the nickel surface. A higher coverage allows a thick thiophene layer to be formed, but heating this to 270 K produces again a NEXAFS spectrum characteristic of atomic sulphur. However, on the surface that had been pre-dosed with oxygen, the low-exposure spectrum (figure 24(d)) looks like that of the thick thiophene layer, with only resonances B and D observed. This, and the fact that no sulphur remains on the surface after heating (figure 24(f)), unambiguously proves that thiophene does not dissociate on the  $c(2 \times 2)$  O-covered Ni(100) surface. These findings are reinforced by the accompanying SEXAFS measurements, which show dominant FT peaks due to short ( $\approx 1.71$  Å) S–C bonds for the  $C_4H_4S$  multi-layer and after adsorption on the oxygen pre-dosed surface, and longer ( $\approx 2.22$  Å) S–Ni bonds for thiophene on clean nickel, the same as for atomic sulphur adsorption.

These studies suggest a site-dependent C–S bond-breaking process. On the clean Ni(100) surface, sulphur is broken out of the thiophene ring by bonding to fourfold hollow nickel sites, and this happens even at temperatures as low as 100 K. The dissociated thiophene layer passivates the surface and higher exposures then form layers of intact thiophene molecules. When half of the active fourfold hollow sites on the nickel surface are blocked by oxygen atoms, no thiophene dissociation occurs. The hydrodesulphurisation process, involving the breaking of C–S bonds in polyatomic organic molecules, is of great industrial importance. These experiments show that x-ray absorption measurements can help to elucidate the nature of such processes for model systems of small molecules on single-crystal surfaces.

## 6. Summary

I have attempted to demonstrate by selectively reviewing some of the many published examples, that x-ray absorption measurements may yield key information on the local bonding configuration at surfaces, either clean or with adsorbed atoms or molecules. An understanding of the basic physical principles is an essential pre-requisite, but the techniques have found application in areas some way distant from mainstream solid state physics.

## Acknowledgments

I am pleased to acknowledge that I have benefited considerably from many discussions on various aspects of x-ray absorption at surfaces with Joachim Stöhr, Paul Citrin, Paul Durham and David King.

## References

- Allyn C L, Gustafsson T and Plummer E W 1977 *Chem. Phys. Lett.* **47** 127–32  
Bambynek W, Crasemann B, Fink R W, Freund H-U, Mark H, Swift C D, Price R E and Rao P V 1972 *Rev. Mod. Phys.* **44** 716–813  
Barrus D M, Blake R L, Burek A J, Chambers K C and Pregonzer A L 1979 *Phys. Rev. A* **20** 1045–61  
Batra I P and Kleinman L 1984 *J. Electron Spectrosc.* **33** 175–241  
Brennan S 1982 *PhD Thesis* Stanford University  
Citrin P H 1985 *Phys. Rev. B* **31** 700–21  
Citrin P H, Eisenberger P and Hewitt R C 1978 *Phys. Rev. Lett.* **41** 309–12  
Citrin P H, Eisenberger P and Kincaid B M 1976 *Phys. Rev. Lett.* **36** 1346–9  
Citrin P H, Eisenberger P and Rowe J E 1982 *Phys. Rev. Lett.* **48** 802–5  
Comin F, Incoccia L, Lagarde P, Rossi G and Citrin P H 1985 *Phys. Rev. Lett.* **54** 122–5  
Davenport J W 1976 *Phys. Rev. Lett.* **36** 945–9  
Dehmer J L and Dill D 1975 *Phys. Rev. Lett.* **35** 213–5  
Döbler U, Baberschke K, Haase J and Puschmann A 1984 *Phys. Rev. Lett.* **52** 1437–40  
Durham P J, Pendry J B and Hodges C H 1982 *Comput. Phys. Commun.* **25** 193–206  
Eisenberger P and Brown G S 1979 *Solid State Commun.* **29** 481–4  
El-Mashri S M, Jones R G and Forty A J 1983 *Phil. Mag. A* **48** 665–83  
Flodström S A, Bachrach R Z, Bauer R S and Hagström S B M 1976 *Phys. Rev. Lett.* **37** 1282–5  
Fox R and Gurman S J 1980 *J. Phys. C: Solid State Phys.* **13** L249–53  
Gurman S J, Binsted N and Ross I 1984 *J. Phys. C: Solid State Phys.* **17** 143–51  
Hayes T M and Boyce J B 1982 *Solid State Phys.* **37** 173–351 (New York: Academic)

- Heald S M, Keller E and Stern E A 1984 *Phys. Lett.* **103A** 155–8
- Heald S M and Stern E A 1977 *Phys. Rev. B* **16** 5549–59
- 1978 *Phys. Rev. B* **17** 4069–81
- Horsley J A, Stöhr J, Hitchcock A P, Newbury D C, Johnson A L and Sette F 1985 *J. Chem. Phys.* **83** 6099–107
- Hussain Z, Umbach E, Shirley D A, Stöhr J and Feldhaus J 1982 *Nucl. Instrum. Methods* **195** 115–31
- Jaeger R, Feldhaus J, Haase J, Stöhr J, Hussain Z, Menzel D and Norman D 1980 *Phys. Rev. Lett.* **45** 1870–3
- Jaeger R, Stöhr J and Kendelewicz T 1983 *Phys. Rev. B* **28** 1145–7
- Jaeger R, Stöhr J, Treichler R and Baberschke K 1981 *Phys. Rev. Lett.* **47** 1399–4
- Johansson L I and Stöhr J 1979 *Phys. Rev. Lett.* **43** 1882–5
- Johnson A L, Muettertities E L and Stöhr J 1983 *J. Am. Chem. Soc.* **105** 7183–5
- Jona F 1978 *J. Phys. C: Solid State Phys.* **11** 4271–306
- Jona F and Marcus P M 1980 *J. Phys. C: Solid State Phys.* **13** L477–80
- Kevan S D, Rosenblatt D H, Denley D, Lu B-C and Shirley D A 1978 *Phys. Rev. Lett.* **41** 1565–8
- Knotek M L 1984 *Rep. Prog. Phys.* **47** 1499–561
- Knotek M L and Feibelman P J 1978 *Phys. Rev. Lett.* **40** 964–7
- Lamble G M, Brooks R, Ferrer S, King D A and Norman D 1986a *Phys. Rev. B* at press
- Lamble G M, Brooks R, King D A and Norman D 1986b *Phys. Rev. B* at press
- Lee P A 1976 *Phys. Rev. B* **13** 5261–70
- Lee P A, Citrin P H, Eisenberger P and Kincaid B M 1981 *Rev. Mod. Phys.* **53** 769–806
- Lee P A and Pendry J B 1975 *Phys. Rev. B* **11** 2795–811
- Ludeke R and Koma A 1975 *Phys. Rev. Lett.* **34** 1170–3
- Lukirskii A P and Brytov I A 1964 *Sov. Phys.—Solid State* **6** 33–41
- MacDowell A A, Norman D and West J B 1985 *Daresbury Laboratory Technical Memorandum* TM 48E
- Martens G and Rabe P 1980 *Phys. Status Solidi a* **58** 415–24
- Martinson C W B, Flodström S A, Rundgren J and Westrin P 1979 *Surf. Sci.* **89** 102–13
- Mott N F and Jones H 1936 *The Theory of the Properties of Metals and Alloys* (Oxford: Clarendon)
- Natoli C R 1982 *EXAFS and Near Edge Structure* (Berlin: Springer) pp 43–56
- Neve J, Rundgren J and Westrin P 1982 *J. Phys. C: Solid State Phys.* **15** 4391–401
- Noguera C and Spanjaard D 1981 *Surf. Sci.* **108** 381–96
- Norman D, Brennan S, Jaeger R and Stöhr J 1981 *Surf. Sci.* **105** L297–306
- Norman D and Durham P J 1983 *SPIE Proc.* **447** 102–6
- Norman D, Stöhr J, Jaeger R, Durham P J and Pendry J B 1983 *Phys. Rev. Lett.* **51** 2052–5
- Owen I W, Brookes N B, Richardson C H, Warburton O R, Quinn F M, Norman D and Thornton G 1986 *Surf. Sci.* at press
- Pauling L 1960 *The Nature of the Chemical Bond* (New York: Cornell University Press)
- Payling R and Ramsey J A 1980 *J. Phys. C: Solid State Phys.* **13** 505–15
- Pettifer R F 1979 in *Trends in Physics 1978* (Bristol: Hilger) pp 522–32
- Piancastelli M N, Ferrett T A, Lindle D W and Shirley D A 1985 unpublished
- Pianetta P, Lindau I, Garner C M and Spicer W E 1975 *Phys. Rev. Lett.* **35** 1356–9
- Rothberg G M, Choudhary K M, den Boer M L, Williams G P, Hecht M H and Lindau I 1984 *Phys. Rev. Lett.* **53** 1183–6
- Sette F, Stöhr J and Hitchcock A P 1984 *J. Chem. Phys.* **81** 4906–14
- Soria F, Martinez V, Muñoz M C and Sacedon J L 1981 *Phys. Rev. B* **24** 6926–35
- Stern E A, Bunker B A and Heald S M 1980 *Phys. Rev. B* **21** 5521–39
- Stöhr J 1986 in *X-Ray Absorption: Principles, Applications, Techniques of EXAFS, SEXAFS and XANES* ed. R Prins and D C Koningsberger (New York: Wiley)
- Stöhr J, Baberschke K, Jaeger R, Treichler R and Brennan S 1981 *Phys. Rev. Lett.* **47** 381–5
- Stöhr J, Gland J L, Eberhardt W, Outka D, Madix R J, Sette F, Koestner R J and Döbler U 1983 *Phys. Rev. Lett.* **51** 2414–7
- Stöhr J, Gland J L, Kollin E B, Koestner R J, Johnson A L, Muettertities E L and Sette F 1984a *Phys. Rev. Lett.* **53** 2161–4
- Stöhr J and Jaeger R 1982 *Phys. Rev. B* **26** 4111–31
- 1983 *Phys. Rev. B* **27** 5146–9
- Stöhr J, Jaeger R, Feldhaus J, Brennan S, Norman D and Apai G 1980a *Appl. Opt.* **19** 3911–9
- Stöhr J, Jaeger R and Kendelewicz T 1982 *Phys. Rev. Lett.* **49** 142–5
- Stöhr J, Johansson L I, Brennan S, Hecht M and Miller J N 1980b *Phys. Rev. B* **22** 4052–65
- Stöhr J, Kollin E B, Fischer D A, Hastings J B, Zaera F and Sette F 1985 *Phys. Rev. Lett.* **55** 1468–71

- Stöhr J, Noguera C and Kendelewicz T 1984b *Phys. Rev. B* **30** 5571–9  
Stöhr J, Sette F and Johnson A L 1984c *Phys. Rev. Lett.* **53** 1684–7  
Teo B-K and Lee P A 1979 *J. Am. Chem. Soc.* **101** 2815–32  
Upton T H and Goddard W A 1981 *Phys. Rev. Lett.* **46** 1635–9  
Wallace S and Dill D 1978 *Phys. Rev. B* **17** 1692–9  
Woodruff D P, Norman D, Holland B W, Smith N V, Farrell H H and Traum M M 1978 *Phys. Rev. Lett.* **41** 1130–3  
Yu H L, Muñoz M C and Soria F 1980 *Surf. Sci.* **94** L184–90